Lithos 360–361 (2020) 105447

Contents lists available at ScienceDirect

Lithos

journal homepage: www.elsevier.com/locate/lithos

Research article

Remnants of a Middle Triassic island arc on western margin of South China Block: Evidence for bipolar subduction of the Paleotethyan Ailaoshan Ocean

Jian Xu [a,b], Xiao-Ping Xia [a,*], Keda Cai [c], Chun-Kit Lai [d], Xi-Jun Liu [e], Qing Yang [a], Mei-Ling Zhou [a,f], Peng-Fei Ma [a,b], Le Zhang [a,b]

[a] State Key Laboratory of Isotope Geochemistry, Guangzhou Institute of Geochemistry, Chinese Academy of Sciences, Guangzhou 510640, China
[b] College of Earth and Planetary Sciences, University of Chinese Academy of Sciences, Beijing 100049, China
[c] State Key Laboratory of Geological Processes and Mineral Resources, School of Earth Science and Resources, China University of Geosciences, Beijing 100083, China
[d] Faculty of Science, Universiti Brunei Darussalam, Gadong, Brunei
[e] Guangxi Key Laboratory of Hidden Metallic Ore Deposits Exploration, Guilin University of Technology, Guilin 541004, China
[f] Southern Marine Science and Engineering Guangdong Laboratory, Zhuhai 519000, China

ARTICLE INFO

Article history:
Received 24 December 2019
Received in revised form 25 February 2020
Accepted 26 February 2020
Available online 29 February 2020

Keywords:
Triassic arc remnant
High-grade metamorphic complex
Bipolar subduction
Ailaoshan tectonic zone
Paleotethys Ocean

ABSTRACT

Identifying ancient magmatic arcs in collisional orogens is important for regional tectonic reconstruction. Here, we first identified Middle Triassic (ca. 235–237 Ma) arc-type hornblende diorite and granodiorite in the Ailaoshan high-grade metamorphic belt in SW China, east of the Paleotethyan Ailaoshan-Song Ma suture. These rocks show arc-type geochemical affinities, such as large-ion lithophile element (LILE; e.g., Rb and Ba) enrichments and high-field-strength element (HFSE; e.g., Nb, Ta and Ti) depletions. They are characterized by positive εNd(t) (+2.90 to +4.63), εHf(t) (+9.9 to +14.1), and higher $\delta^{18}O$ (mean 6.35–6.65‰) than typical mantle-derived magmas. Whole-rock geochemical and Sr-Nd-Hf-O isotope data demonstrate that the hornblende diorite was derived from depleted MORB-like mantle metasomatized by subducted oceanic sediments, and the granodiorite was formed by fractional crystallization from mafic magmas. These two rock types likely represent remnants of a continental arc, whose upper arc architecture may have been mostly-/completely-eroded by the subsequent Indosinian (Triassic) and Himalayan (Cenozoic) orogenic events. Tectonically, the presence of Triassic arc remnants east of the Paleotethyan Ailaoshan-Song Ma suture suggests the occurrence of east-dipping (present orientation) subduction of the Paleotethys beneath the South China Block, a hypothesis discarded by most previous studies due to the lack of arc magmatic evidence. Combined with previous studies in the Ailaoshan tectonic zone and its southern extension (Song Ma tectonic zone), we propose that the Paleotethyan Ailaoshan Ocean may have been bipolar-subducted westward and eastward beneath the Indochina and South China blocks, respectively.

1. Introduction

Mass exchange in subduction zones between the mantle and surficial geochemical reservoir (e.g., ocean, crustal rocks and sediments) gives rise to arc-type magmas (Chauvel et al., 2008). Most arc magmas are thought to be originated from partial melting of the sub-arc mantle wedge metasomatized by subducting slab-derived fluids and/or silicate melts (e.g., Hawkesworth et al., 1993; Plank and Langmuir, 1998). These arc-type rocks are characterized by distinctive isotopic and geochemical compositions, such as enrichment in large ion lithophile element (LILE) and depletion in high field strength element (HFSE). Mafic-felsic plutons in ancient orogenic belts may represent remnants of the magmatic arc root, e.g., the Permian Gympie Group in eastern Australia is interpreted as volcanic arc remnants (e.g., Sivell and Waterhouse, 1988). Remnants of the magmatic arc root are commonly metamorphosed and tectonically disrupted due to the later thermotectonic overprinting. Identification of these arc remnants in ancient orogenic belts is vital for reconstructing oceanic subduction history and the assembly and break up of supercontinents.

Southeast (SE) Asia comprises mainly Gondwana-derived terranes, including the South China, Indochina, Sibumasu, West Burma, Southwest Borneo and West Sumatra (Metcalfe, 2013). The northward drifting and accretion of these terranes onto the Eurasian margin have opened and closed three intervening Paleozoic-Mesozoic oceans, i.e., the Paleotethys, Mesotethys, and Neotethys (e.g., Faure et al.,

* Corresponding author.
E-mail address: xpxia@gig.ac.cn (X.-P. Xia).

https://doi.org/10.1016/j.lithos.2020.105447
0024-4937/

2014; Metcalfe, 2013). Among these three ocean basins, the Paleotethys is the least understood because of the superimposing of Meso- and Neo-Tethyan tectonics (e.g., Liu et al., 2013; Zhang et al., 2017). Remnants of the Paleotethys are preserved in a series of suture zones, i.e., AyimaqinKunlun-Mutztagh suture zone (e.g., Yin and Harrison, 2000), Jinshajiang-Ailaoshan-Song Ma-Song Chay-Hainan suture zone (e.g., Faure et al., 2018; Wang et al., 2000), Longmu Co-Shuanghu, Changning-Menglian and Chiang Mai-Inthanon-Chanthaburi-Bentong-Raub suture zones (e.g., Metcalfe, 2013). The Ailaoshan-Song Ma-Song Chay-Hainan suture in SW China and Vietnam is suggested to represent a branch of the eastern Paleotethys or a late Paleozoic back-arc basin associated with eastward subduction of the Changning-Menglian Paleotethyan main ocean (Fig. 1a) (Fan et al., 2010; Faure et al., 2014; Faure et al., 2018; Wang et al., 2000). The Ailaoshan-Song Ma branch/back arc basin was inferred to be closed in the Triassic (Faure et al., 2014, 2016a, 2016b; Ji et al., 2020; Lepvrier et al., 2004; Liu et al., 2015; Wang et al., 2018; Xu et al., 2019a, 2019b; Zi et al., 2012). After its closure, the region has experienced multiphase tectonic overprint,

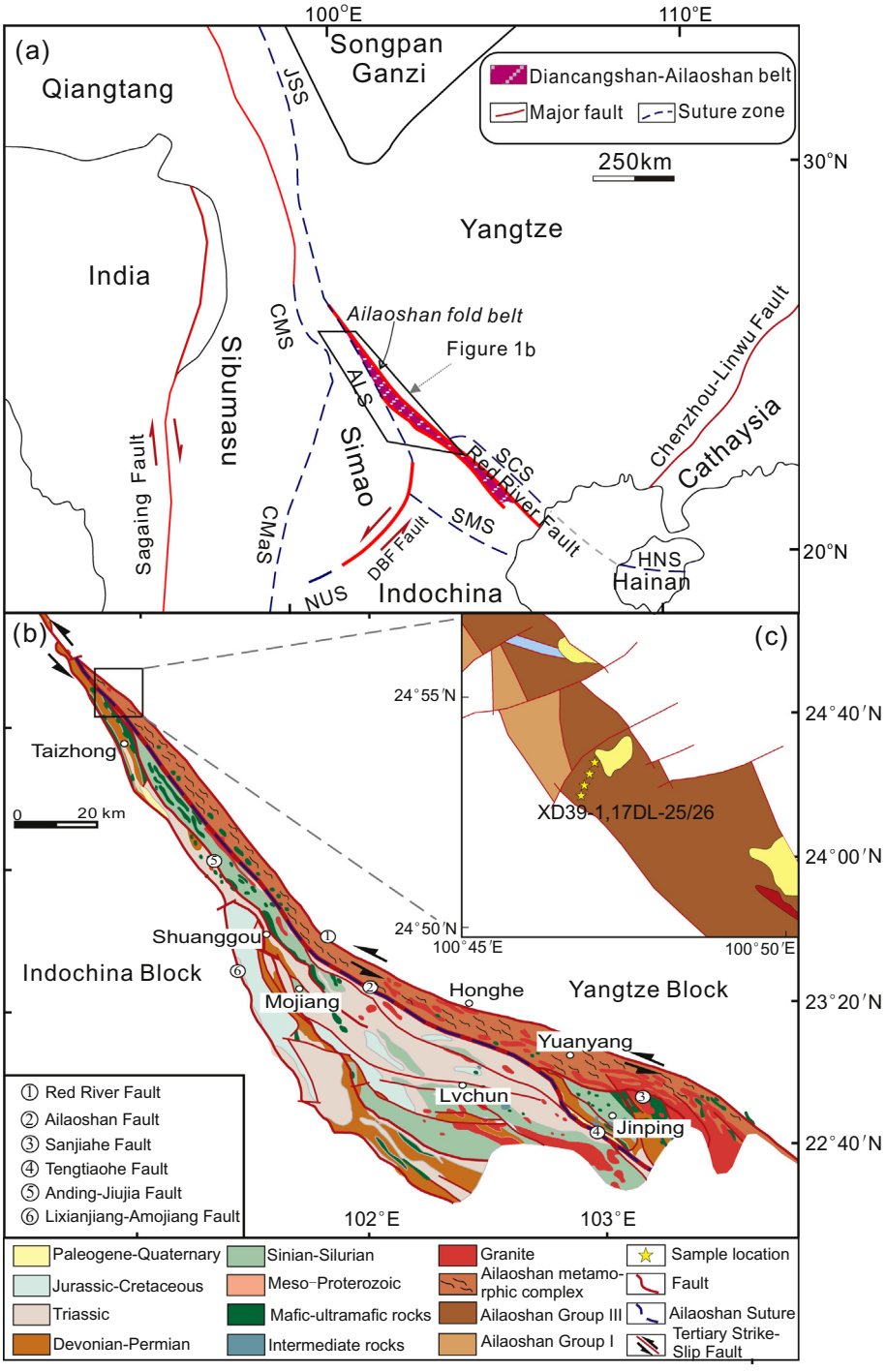

Fig. 1. (a) Simplified tectonic map of SE Asia, showing major sutures and faults (modified after Faure et al., 2018; Xu et al., 2019c). Abbreviations: JSS = Jinshajiang Suture; ALS = Ailaoshan Suture; SMS = Song Ma Suture; SCS = Song Chay Suture; HNS = Hainan Suture; DBP = Dian Bian Phu; CMS = Changling-Menglian Suture; NUS = Nan-Uttaradit Suture; CMaS = Chiang Mai Suture; Emeishan LIP = Emeishan Large Igneous Province. (b) Tectonic outline of the Ailaoshan fold belt (modified after Xu et al., 2019a). Blue dashed line represents location of the Ailaoshan suture zone from Xia et al. (2016). (c) Sketch map of the Ailaoshan metamorphic complex, showing the sampling locations (modified after YNGMR, 1990).

notably the Cenozoic India-Asia collision (Zhang et al., 2017), leading to difficulties in reconstructing the geological evolution of the eastern Paleotethys branch oceans/back arc basin, especially those concerning its subduction polarity. Most studies agreed that the Ailaoshan-Song Ma branch/back-arc basin had subducted westward beneath the Indochina Block, based on the well-preserved Permian-Triassic Taizhong-Lixianjiang and Truong Son arc systems on the eastern margin of Indochina (Halpin et al., 2016; Liu et al., 2011; Liu et al., 2012; Wei and Shen, 1997). East-dipping subduction beneath the South China Block was also proposed, but is mainly supported by Permian-Triassic sedimentary or paleontological (e.g., radiolarian assemblage in Qinfang Basin) evidence in SW South China Block (Hou et al., 2017; Ke et al., 2018; Xu et al., 2019a), yet no direct evidence from arc-type magmatic rocks has ever been presented.

In this study, we first report Middle Triassic arc-type hornblende diorite and granodiorite from the Ailaoshan high grade metamorphic complex, east of the Paleotethyan Ailaoshan suture zone. We present new data on their zircon U—Pb ages and Hf—O isotopes, whole-rock geochemistry and Sr—Nd isotopes, and identify two source components involved in their generation. We argue that these intermediate-felsic plutonic rocks represent remnants of an eroded continental arc sourced from the depleted mantle metasomatized by subducted sediments, and proposed that the eastern Paleotethyans Ailaoshan Ocean was subducted to both eastward and westward beneath the South China and Indochina blocks, respectively.

2. Geological background and sample descriptions

The Ailaoshan fold belt is a NW-SE striking fan-shaped terrane (~500 km long and 20–100 km wide) that narrows to the NW and widens to SE (Fig. 1b) (Faure et al., 2016a). It extends northwest to the Jinshajiang tectonic zone (Yunnan, SW China) (Fig. 1b) (Wang et al., 2000; Wang et al., 2014), with its southeastern extension to the Song Ma tectonic zone (northern Vietnam) (Faure et al., 2018). Situated between the South China (comprising Yangtze and Cathaysia blocks) and Indochina blocks, the Ailaoshan fold belt was variously suggested to be the remnants of an oceanic branch (i.e., Ailaoshan Ocean) or a back-arc basin of eastern Paleotethyan ocean (Fan et al., 2010; Faure et al., 2014; Wang et al., 2000). However, in this study, we infer that the Ailaoshan belt most probably represent the remnants of one Paleotethyan branch ocean based on following facts: (1) Previous isotopic data and geochemical compositions constrained the Devonian Shuanggou ophiolites within the Ailaoshan fold belt being of typical NMORB-type ophiolites comprised of primary pyrolite (lherzolite), relict pyrolite (harzburgite), diabase, gabbro and basalt, which are different from the supra-subduction zone (SSZ) ophiolites (e.g., Xu and Castillo, 2004;); (2) Recent studies have suggested that the Ailaoshan ocean (or back-arc basin) was mainly opened before the Devonian, possible at Silurian, although further rifting in the Late Paleozoic may have occurred (e.g., Liu et al., 2018; Xia et al., 2016).

Several belt-parallel strike-slip faults have divided the Ailaoshan fold belt into elongated and narrow strips (Faure et al., 2016a, 2016b; Fig. 1). From west to east, these tectonic strips and their boundaries include (Lai et al., 2014a, 2014b): Lixianjiang-Amojiang Fault, the western Ailaoshan volcanic belts, Jiujia-Anding Fault, the Ailaoshan ophiolitic mélange, the Ailaoshan Fault, and the Ailaoshan high-grade metamorphic complex, and the Red River Fault.

The western Ailaoshan volcanic belts crops out discontinuously SE, W, and NW of Mojiang (Fig. 1). Three lithological units were recognized in this zone, from bottom to the top include (Faure et al., 2016a): (1) Silurian to Devonian mudstone-siltstone-sandstone turbiditic alternations; (2) Carboniferous to Triassic volcanic and volcanic-sedimentary rocks (Fan et al., 2010; Liu et al., 2011); (3) Late Triassic red beds made of conglomerate, sandstone, and siltstone. The volcanic formation in the belt is comprised of andesite, dacite, rhyolite, basaltic andesite, and high-Al basalt (Faure et al., 2016a), which largely cropped out in the Wusu, Yaxuanqiao and Maoheshan areas, near Mojiang (Fan et al., 2010; Liu et al., 2011). These volcanic rocks are dated from Late Carboniferous to Triassic (287–249 Ma) with arc and/or continental-rift affinities (Fan et al., 2010; Liu et al., 2011), which are commonly attributed to the west-dipping subduction of the Ailaoshan Ocean (Wei and Shen, 1997). Permian-Triassic (257–244 Ma) granitoids reported in the Heping, Pingzhang, Pinghe and Xin'anzhai areas correspond to the plutonic root of the western Ailaoshan magmatic arc (Faure et al., 2016a; Lai et al., 2014a; Liu et al., 2015). The Ailaoshan ophiolitic mélange is bounded by the Jiujia-Anding, and the Ailaoshan faults to the west and East, respectively (Fig. 1). They contain mainly meter- to kilometer-sized blocks of Devonian to Lower Carboniferous serpentinized lherzolite, harzburgite, gabbro, dolerite, plagiogranite, basalt, ribbon-bedded chert, and limestone enclosed into a sandstone-siltstone matrix (Faure et al., 2016a). The Devonian to Carboniferous (ca. 383–334 Ma) gabbro-dolerite-basalt show N-MORB geochemical affinities (Lai et al., 2014b; Xu and Castillo, 2004; YNGMR, 1990), and may have formed in a slow spreading ocean basin.

The location of the South China-Indochina suture been proposed to be the Lixianjiang-Amojiang fault based on the distribution of the Emeishan basalts in Jinping within the high-grade metamorphic complex (Chung et al., 1997). More recently, comprehensive detrital zircon U—Pb dating and Hf isotope analyses on the Paleozoic sedimentary rocks across the belt have suggested that the Ailaoshan ophiolite belt (Wang et al., 2014) or the Ailaoshan-Tengtiaohe fault (Xia et al., 2016) may represent the location of the Ailaoshan suture.

The Ailaoshan high-grade metamorphic complex was likely first formed by the Triassic collision between the South China and Indochina blocks (Fig. 1b). It mainly comprises of different kinds of paragneiss, schist, quartzite, marble and amphibolite (Liu et al., 2013; YNGMR, 1990). This metamorphic complex had been originally regarded as the Precambrian crystalline basement of the Yangtze Block (YNGMR, 1990). However, recent studies indicated that the metamorphic complex contains rocks ranging from Neoproterozoic to Tertiary (820–25 Ma) (Ji et al., 2020; Lin et al., 2012; Liu et al., 2013; Qi et al., 2012). Comprehensive geochronological studies on the meta-igneous/—sedimentary rocks (e.g., schist, paragneiss, and amphibolite) from the Ailaoshan complex revealed multiple metamorphic events (Ji et al., 2020; Liu et al., 2013): (1) the Early-Late Triassic (249–222 Ma) high-pressure metamorphic rocks in the Dali, Gasa, Yuanjiang and Honghea areas are associated with the subduction-closure of the Paleotethys, which may indicate the final closure of the Ailaoshan Ocean in the Late Triassic (Ji et al., 2020; Lin et al., 2012; Liu et al., 2013). (2) Eocene-Oligocene (44–14 Ma) metamorphic rocks in Gasa, Mosha, Yuanjiang and Honghe areas are associated with the sinistral ductile deformation along the Ailaoshan-Red River (ASRR) shear zone (Ji et al., 2020; Lin et al., 2012; Liu et al., 2013). Inherited detrital zircons (528 Ma to 2550 Ma) were also reported from those rocks, which may record widespread geological events throughout the Gondwana supercontinent (Ji et al., 2020; Liu et al., 2013). Permian-Triassic (280–233 Ma) granitoids have also been reported from the complex (Lin et al., 2012; Liu et al., 2017a; Wu et al., 2016), but were interpreted as continental rift or Indochina-South China collision-related (Liu et al., 2017a; Wu et al., 2016). More recently, Xu et al. (2019c) reported Late Permian (ca. 261 Ma) Nb-enriched basalts (NEBs) from the Ailaoshan metamorphic complex, which geochemically mimic the NEBs from typical intracontinental back-arc basin setting. However, Permian-Triassic arc magmatic rocks were yet to be discovered.

Our diorite-granodiorite samples were collected from the northern part of the Ailaoshan high-grade metamorphic complex, near the town of Taizhong (N 24°52.78′–24°52.85′, E 100°47.36′–100°47.40′; Fig. 1c). The diorite-granodiorite intruded the Paleozoic Ailaoshan Group (Fig. 2a and b), indicating that they are native rather than exotic blocks. Only the least altered rocks were sampled. The hornblende diorites are composed of hornblende (50–55%), plagioclase (35–40%), biotite (~5%) and accessory (<5%) epidote, zircon, apatite and magnetite

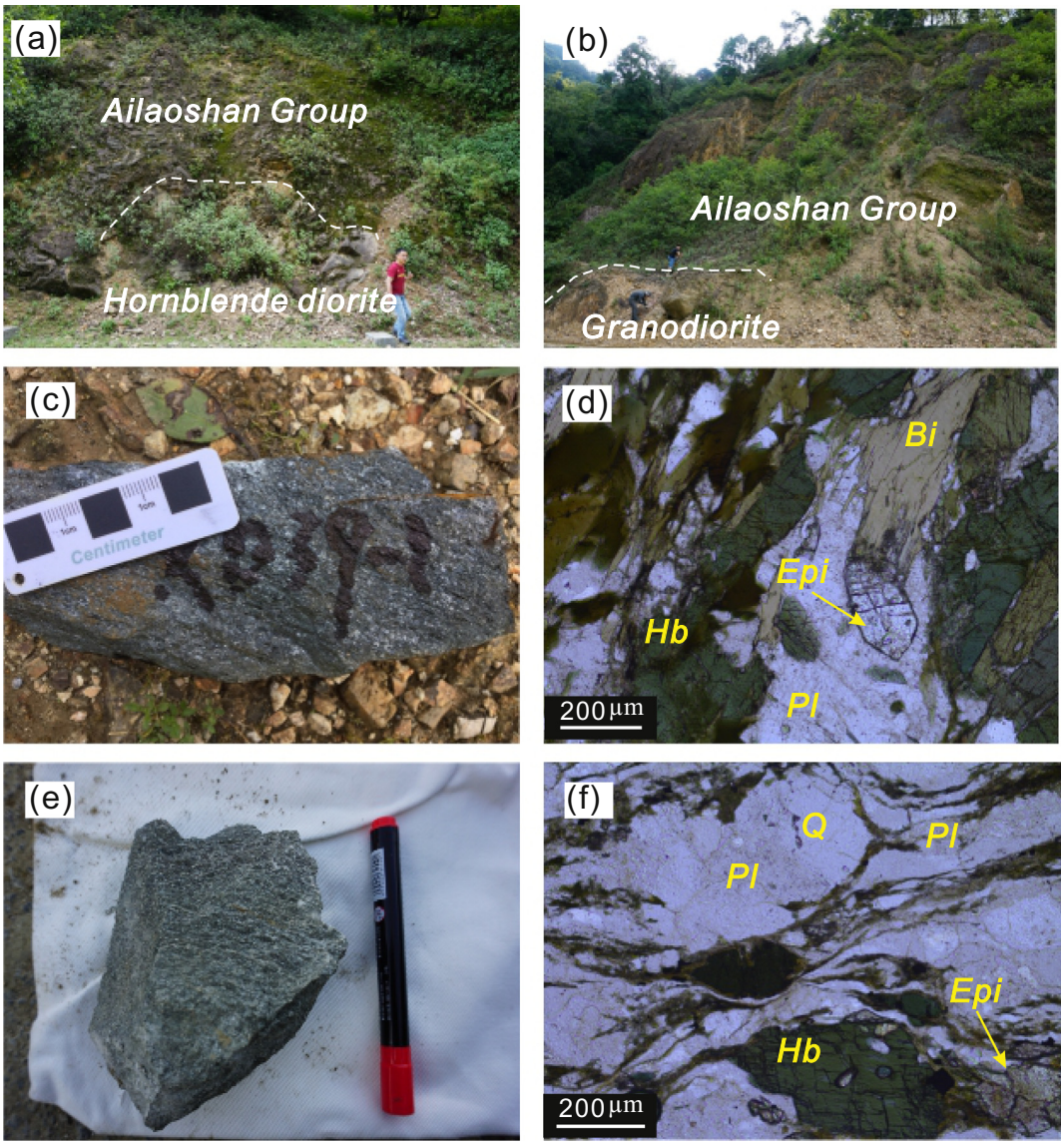

Fig. 2. Representative field photographs and photomicrographs of the Ailaoshan hornblende diorites and granodiorites in the Ailaoshan metamorphic complex. Outcrop of the hornblende diorite (a) and the granodiorites (b); (c) Dark-grey hornblende diorites (Sample XD39–1); (d) Hornblende, plagioclase, biotite and euhedral epidote in hornblende diorites (plane-polarized light); (e) Greyish-green granodiorites (Sample 17DL-26E); (f) Plagioclase, quartz and minor epidote and hornblende in granodiorites (plane-polarized light). Mineral abbreviations: Hb = hornblende; Bi = biotite; Epi = epidote; Pl = plagioclase; Q = quartz.

(Fig. 2c and d). The hornblende is mostly subhedral and shows distinct pleochroism, whilst the plagioclase occurs mainly as subhedral laths. The granodiorites are fine-medium grained (Fig. 2e), and contain mainly plagioclase (65–70%) and quartz (15–20%), and minor K-feldspar (~5%), hornblende (<5%) and biotite (<3%), and trace (<5%) zircon, epidote and Fe—Ti oxides. The plagioclase occurs as subhedral laths with well-developed twinning, whilst the hornblende is subhedral and shows distinct pleochroism (Fig. 2f). Both the hornblende diorite and granodiorite have experienced minor deformation, as shown by weak foliation in the hand specimens (Fig. 2c and e).

3. Analytical methods

3.1. Zircon U—Pb age and O isotope analyses

Secondary ion mass spectrometry (SIMS) zircon U—Pb analyses were conducted using a CAMECA IMS1280-HR system at the State key Laboratory of Isotope Geochemistry, Guangzhou Institute of Geochemistry, Chinese Academy of Sciences (SKLaBIG, GIG-CAS). The analytical procedure was the same as that described in Li et al. (2009). The ellipsoidal spot is about 20 μm × 30 μm in size. Calibration of Pb/U ratios is relative to the standard zircon Plesovice (337.13 Ma) (Sláma et al., 2008), which was analyzed once every four unknowns, based on an observed linear relationship between ln ($^{206}Pb/^{238}U$) and *ln* ($^{238}U^{16}O_2/^{238}U$). A long-term uncertainty of 1.5% (1 RSD) for $^{206}Pb/^{238}U$ measurements of the standard zircons was propagated to the unknowns (Li et al., 2010a), despite that the measured $^{206}Pb/^{238}U$ error in a specific session is generally around 1% (1 RSD) or less. U and Th concentrations of the unknowns were also calibrated relative to the standard zircon Plesovice, with its Th and U concentrations of 78 ppm and 755 ppm, respectively (Sláma et al., 2008). Measured compositions were corrected for common Pb using non-radiogenic ^{204}Pb. A secondary standard zircon Qinghu (Li et al., 2013) was analyzed as unknown to monitor the reliability of the whole procedure. Uncertainties on single analyses are reported at the 1σ level; mean ages for pooled U—Pb analyses are quoted with 95% confidence interval.

Zircon oxygen isotopes were measured using the same CAMECA IMS1280-HR SIMS at the SKLaBIG, GIG-CAS. The $133Cs^+$ primary ion

beam was accelerated at 10 kV, with an intensity of ~2 nA and focused to an area of ϕ 10 μm on the sample surface and the size of analytical spots is about 20 μm in diameter (10 μm beam diameter +10 μm raster). Oxygen isotopes were measured in multi-collector mode using two off-axis Faraday cups. The measured oxygen isotopic data were corrected for instrumental mass fractionation (IMF) using the Penglai zircon standard ($\delta^{18}O_{VSMOW}$ = 5.3‰; Li et al., 2010b), which was analyzed once every four unknowns, using sample-standard bracketing (SSB) method. The internal precision of a single analysis generally was better than 0.1‰ (1σ) for the $^{18}O/^{16}O$ ratio. As discussed by Valley and Kita (2009), internal precision for a single spot (commonly <0.1‰, 1σ) is not a good index of analytical quality for stable isotope ratios measured by SIMS. Therefore, the external precision, measured by the spot-to-spot reproducibility of repeated analyses of the Penglai standard, 0.30‰ (2σ, n = 24) is adopted for data evaluation. Fifteen measurements of the Qinghu zircon standard during the course of this study yielded a weighted mean of $\delta^{18}O$ = 5.6 ± 0.10‰ (2σ), which is consistent with the reported value of 5.4 ± 0.2‰ within analytical errors (Li et al., 2013).

3.2. Zircon Lu—Hf isotope analyses

All zircon Hf isotope analyses in this study were performed on a Neptune Plus MC-ICP-MS (Thermo Scientific), coupled with a RESOlution M-50193 nm laser ablation system (Resonetics), which are hosted at the SKLaBIG, GIG-CAS. The detailed description of the two instruments can be found in Zhang et al. (2014a). An X skimmer cone in the interface and a small flow of N_2 (2ml L^{-1}) were used to improve the instrumental sensitivity. All isotope signals are detected with Faraday cups under static mode. The laser parameters were set as follow: beam diameter, 45 μm; repetition rate, 6 Hz; energy density, ~4 J cm^{-2}. Helium was chosen as the carrier gas (800 ml min^{-1}). A "squid" smoothing device on the gas line to the ICP gives a smooth signal. Each analysis consisted of 400 cycles with an integration time of 0.131 s per cycle. The first 28 s was used to detect the gas blank with the laser beam off, followed by 30 s laser ablation for sample signals collection with laser beam on. During the measurement of this study, the gas blank of ^{180}Hf was less than 0.2 mv. ^{173}Yb and ^{175}Lu were used to correct the isobaric interference of ^{176}Yb and ^{176}Lu on ^{176}Hf. The natural ratio values of $^{176}Yb/^{173}Yb$ and $^{176}Lu/^{175}Lu$ used in the correction are 0.79381 and 0.02656 (Segal et al., 2003). The mass bias factor of Yb is calculated from the measured $^{173}Yb/^{171}Yb$ and the natural ratio of 1.13268. The mass bias factor of Lu is assumed to be the same as that of Yb. The mass bias of $^{176}Hf/^{177}Hf$ was normalized to $^{179}Hf/^{177}Hf$ = 0.7325 with an exponential law. The detailed data reduction procedure is reported in Zhang et al. (2015). 40 analyses of the Plešovice zircon during the course of this study yielded a weighted mean of $^{176}Hf/^{177}Hf$ = 0.282483 ± 0.000035 (2SD), which is consistent within errors with the reported value in Sláma et al. (2008).

3.3. Whole-rock major- and trace-element analyses

The least-altered samples selected for geochemical analyses were powdered to ~200-mesh in an agate mortar. Major elements of samples were analyzed on the fused glass beads using Rigaku ZSX PrimusIIX-ray fluorescence (XRF) spectrometer at the Chinese Academy of Science (CAS) Key Laboratory of Crust–Mantle Materials and Environments at University of Science and Technology of China (USTC), Hefei and Wuhan Samplesolution Analytical Technology Co., Ltd., Wuhan. A preignition method was used to determine the loss on ignition (LOI) prior to major element analyses. Analytical results for the GBW reference standards (GBW07103, GBW07111and GBW07112) and the U.S. Geological Survey (USGS) reference standards (GSR-1, GSR-2, and GSR-3) indicate that the analytical uncertainties were generally less than 2%. Trace elements were analyzed using a Perkin-Elmer ELAN 6000 inductively-coupled plasma source mass spectrometer (ICP-MS) at the SKLaBIG, GIG-CAS. Analytical procedures are similar to those described in Li et al. (2006a). The USGS reference standards (BHVO-2, AVG-2, GSR-1, GSR-2, GSR-3, GSD-9, and SARM-4) were chosen as external calibration standards for calculating the elemental concentrations in the measured samples. Analytical precision and accuracy are better than 3%.

3.4. Whole-rock Sr—Nd isotope analyses

Whole-rock Sr and Nd isotopic analyses of selected samples were performed using a Micromass Isoprobe multi-collector mass spectrometer (MC-ICPMS) at SKLaBIG, GIG-CAS, using analytical procedures described by Li et al. (2006a). The reported $^{87}Sr/^{86}Sr$ and $^{143}Nd/^{144}Nd$ ratios were respectively adjusted to the NBS987 standard $^{87}Sr/^{86}Sr$ = 0.71025 and the Shin Etsu JNdi-1 standard ($^{143}Nd/^{144}Nd$ = 0.512115). All the measured $^{87}Sr/^{86}Sr$ and $^{143}Nd/^{144}Nd$ ratios were normalized to $^{86}Sr/^{88}Sr$ = 0.1194 and $^{146}Nd/^{144}Nd$ = 0.7219, respectively.

3.5. Mineral composition analyses

Major elements of amphibole, plagioclase and epidote were determined using a JEOL JXA-8230 electron probe micro-analyzer (EPMA) at the Key Laboratory of Mineralogy and Metallogeny of GIGCAS. Operating conditions for all elements include 15 kV accelerating voltage, 20 nA beam current, 1 μm beam size. Peak and background counting time is 10 s for most elements. Analytical results were reduced using the ZAF correction routine.

4. Results

4.1. Zircon U—Pb dating

One hornblende diorite (XD39–1) and one granodiorite (17DL-26A) were selected for zircon U—Pb dating. For the hornblende diorite, zircon grains (size: 100–200 μm; length/width ratios: 1.5–2.0) exhibit broad oscillatory zoning and high Th/U ratios (0.3–1.5), indicating a magmatic origin (Corfu et al., 2003). Thirteen analyses yielded a weighted mean $^{206}Pb/^{238}U$ age of 235 ± 2 Ma (MSWD = 1.08) (Fig. 3a; Supplementary Table S1), representing the age of the hornblende diorite emplacement. For the granodiorite, zircon grains (size: 60–120 μm; length/width ratio: 1.2–2.0) exhibit broad oscillatory zoning and high Th/U ratios (0.4–0.8), also indicating a magmatic origin (Corfu et al., 2003). Fifteen analyses yielded a weighted mean $^{206}Pb/^{238}U$ age of 237 ± 2 Ma (MSWD = 0.73) (Fig. 3b; Supplementary Table S1), representing the age of the granodiorite emplacement.

4.2. Whole-rock geochemistry

The hornblende diorite samples have SiO_2 and (Na_2O + K_2O) contents of 49.55–54.39 wt% and 5.00–5.26 wt%, respectively, and are subalkaline in the total alkali versus silica (TAS) diagram (Fig. 4a). They are Na-rich (K_2O/Na_2O = 0.31–0.40) and calc-alkaline (Fig. 4b). The rocks have high contents of MgO (4.96–5.99 wt%), total Fe_2O_3 (Fe_2OT 3, 10.12–13.34 wt%), CaO (7.32–8.53 wt%), and Mg# (48–57) (Fig. 4c and d; Supplementary Table S2). In the chondrite-normalized rare earth element (REE) diagram (Fig. 5a), the hornblende diorites show slightly light REE (LREE)-enriched patterns ($(La/Yb)_N$ = 3.09–3.45) and negligible Eu anomalies (Eu/Eu^* = 0.86–0.97) (Supplementary Table S2). In the primitive mantle-normalized multi-element spidergram, the hornblende diorites are characterized by large-ion lithophile elements (LILEs; e.g., Rb and Ba) enrichment and high-field-strength elements (HFSEs; e.g., Nb, Ta and Ti) depletion (Fig. 5b).

The granodiorites contain relatively high SiO_2 (64.64–70.98 wt%) and total alkali contents (6.49–6.92 wt%). These rocks are relatively Na-rich (K_2O/Na_2O = 0.36–0.65) and are calc-alkaline (Fig. 4b). The granodiorites have intermediate contents of Fe_2OT 3 (3.40–5.64 wt%), MgO (0.85–1.58 wt%), CaO (2.54–3.95 wt%) and Mg# (36–41) (Fig. 4c

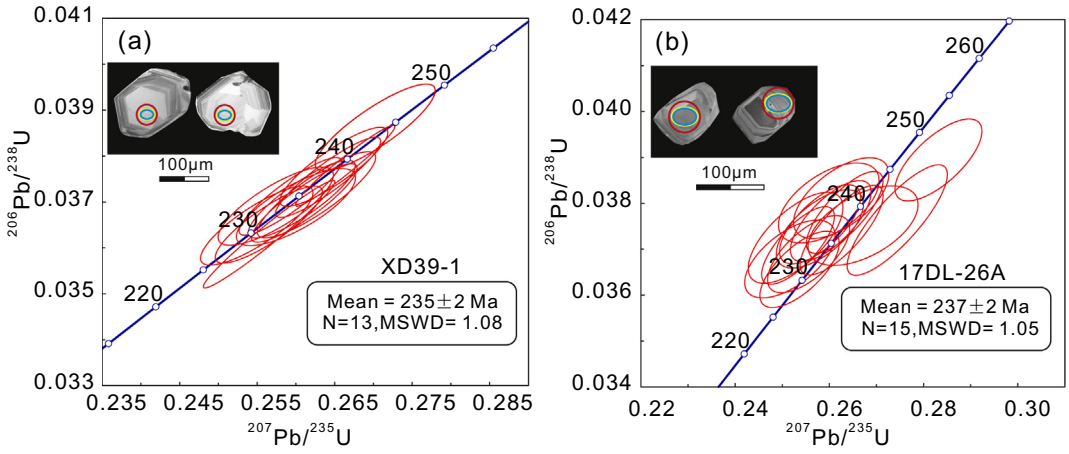

Fig. 3. Secondary Ion Mass Spectroscopy (SIMS) zircon U—Pb concordia diagrams and representative zircon cathodoluminescence (CL) images for the hornblende diorite (a) and granodiorite (b). Circles on zircon grains represent the location of Hf, O isotope analysis and U—Pb dating.

and d; Supplementary Table S2). The aluminum saturation index (ASI; A/CNK = molar $Al_2O_3/(CaO + Na_2O + K_2O)$) varies from 0.97 to 1.04, suggesting that the rocks are metaluminous to weakly peraluminous (Supplementary Table S2). The granodiorites display LREE-enriched chondrite-normalized REE patterns ($(La/Yb)_N$ = 4.66–6.82) and have negative Eu anomalies (Eu/Eu* = 0.81–0.84) (Fig. 5c). In the primitive mantle-normalized multi-elements spidergram (Fig. 5d), they are enriched in LILEs and depleted in HFSEs, similar to the hornblende diorites. The granodiorites show negative Sr anomalies, whilst the hornblende diorites show positive Sr anomalies.

4.3. Whole rock Sr—Nd and zircon Hf—O isotopes

The hornblende diorites exhibit low and nearly constant ($^{87}Sr/^{86}Sr)_i$ values (0.7046–0.7050) and uniform εNd(t) values (+3.63 to +4.22) (Fig. 6a; Supplementary Table S2). The granodiorites have low and varying ($^{87}Sr/^{86}Sr)_i$ values (0.7037–0.7046), and similar εNd(t) values (+2.90 to +4.63) to those of the hornblende diorites (Fig. 6a; Supplementary Table S2).

Zircon grains from hornblende diorite have similarly positive εHf (t) values (+9.9 to +12.6) and Hf modal ages (T_{DM2} = 261–289 Ma)

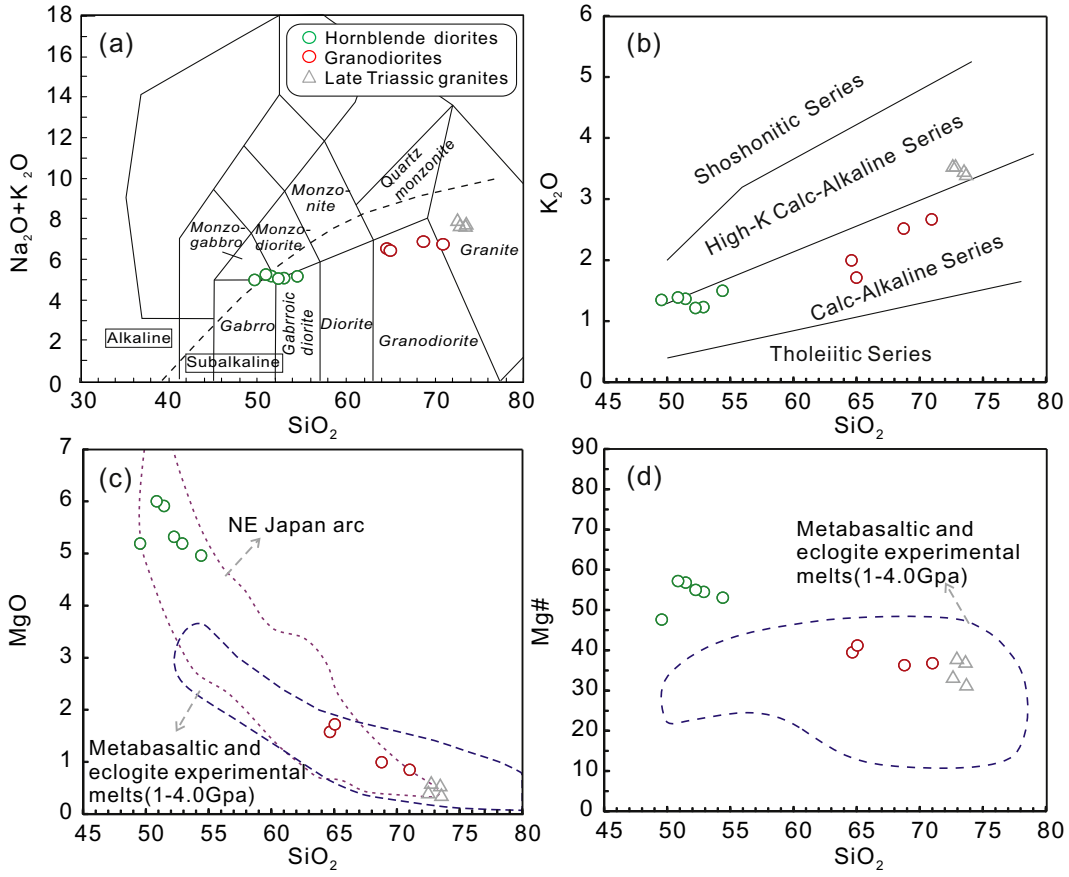

Fig. 4. (a) SiO_2 versus $K_2O + Na_2O$ diagram showing classification of the hornblende diorites and granodiorites from the Ailaoshan metamorphic complex. Plots of (b) K_2O versus SiO_2; (c) MgO versus SiO_2 and (d) Mg# versus SiO_2. Data of Late Triassic granites for comparison are from Liu et al. (2014).

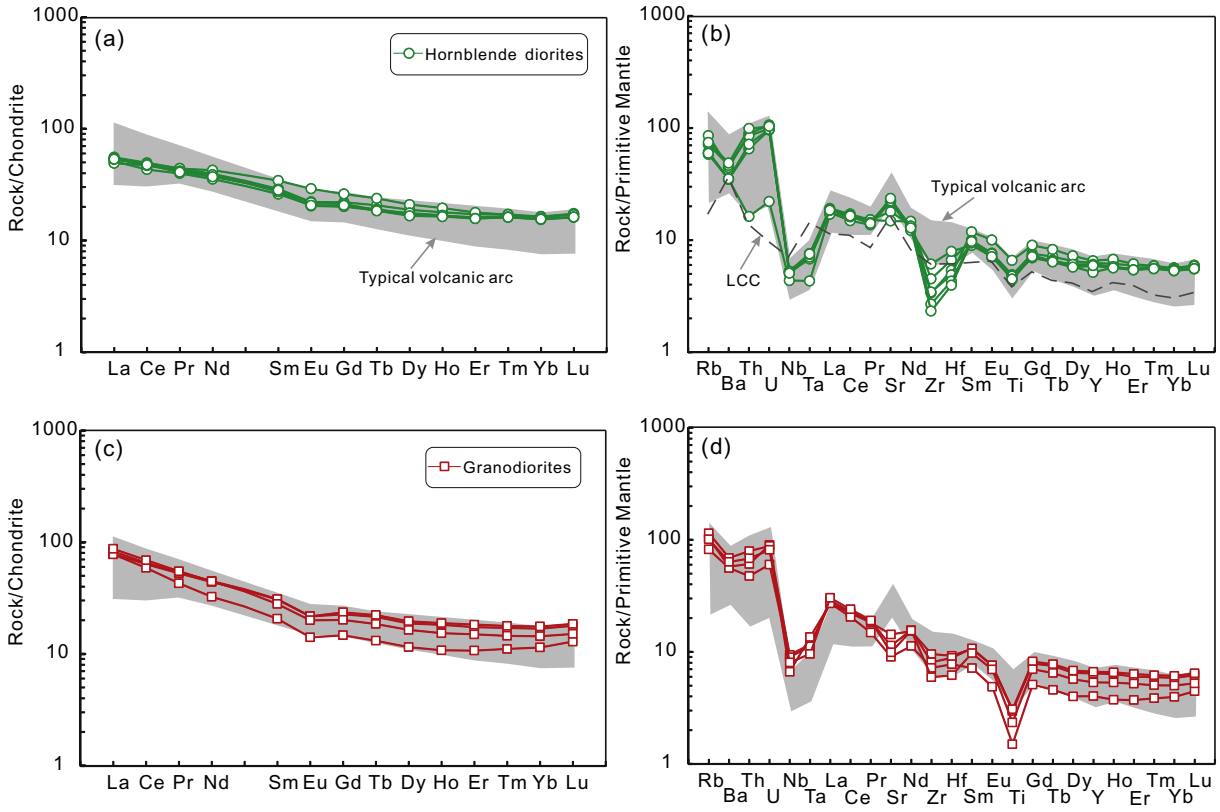

Fig. 5. Chondrite-normalized rare earth elements (REEs) and primitive mantle-normalized multi-element diagrams for the hornblende diorites (a-b) and granodiorites (c-d). Normalizing values are from Sun and McDonough (1989). Average compositions of the lower continental crust (LCC) are from Rudnick and Gao (2003).

to those of the granodiorite ($\varepsilon Hf(t) = +9.9$ to $+14.1$; $T_{DM2} =$ 249–288 Ma) (Fig. 6b; Supplementary Table S3). The hornblende diorite and granodiorite have slightly higher $\delta^{18}O_{zircon}$ values (5.76–6.59‰ (mean 6.35 ± 0.23‰) and 6.25–7.20‰ (mean 6.65 ± 0.18‰), respectively; Fig. 6c and d) than that of typical igneous zircon in equilibrium with mantle-derived magmas (5.3 ± 0.3‰) (Valley et al., 2005).

4.4. Mineral geochemistry

Representative EPMA results of plagioclase from the hornblende diorite and granodiorite samples are given in Supplementary Table S4. The Plagioclase has relatively low CaO contents of 3.99–6.22 wt% (hornblende diorite) and 3.46–4.62 wt% (granodiorite) (Supplementary Table S4), and is classified as mainly oligoclase with minor andesine ($An_{19-29}Ab_{75-81}Or_{1-2}$ and $An_{17-24}Ab_{70-80}Or_{1-2}$).

5. Discussion

5.1. Petrogenesis of the hornblende diorites

5.1.1. Accumulation and fractional crystallization

The weakly negative Eu anomalies ($Eu/Eu^* = 0.86–0.97$) of the hornblende diorites suggest insignificant accumulation but fractionation of feldspars. In addition, the hornblende diorites have higher concentrations of LILEs and other strongly incompatible elements (e.g., Rb, Ba, Th and U) than the average lower continental crust (LCC) (Fig. 5b) (Rudnick and Gao, 2003), also indicating insignificant hornblende and pyroxene accumulation (Guo et al., 2016). Considering that the hornblende diorites display no obvious cumulate textures (Fig. 2d), our data allow a general assessment of the source characteristics of the magma. The hornblende diorites have lower compatible elements contents (e.g., Cr =17–47 ppm and Ni = 4–17 ppm) and Mg# values (48–57) than those of typical primary mantle-derived melts (Cr > 400 ppm; Ni > 1000 ppm). The rocks also show positive Cr vs. Ni correlation (Fig. 7a), suggesting varying degree of mafic mineral (e.g., clinopyroxene and/or olivine) fractionation. The positive CaO and CaO/Al_2O_3 vs. MgO correlation is consistent with clinopyroxene fractionation (Fig. 7b and inset). Hornblende fractionation is indicated by the positive Y vs. Dy correlation (Fig. 7c). The negative Nb—Ta and Ti anomalies may have been attributed to the fractionation of Ti-rich minerals. However, this could not be the main cause for the significant Nb—Ta anomalies in the hornblende diorites, due to the nearly constant Nb/La ratios (0.27–0.30) with respect to the varyingTiO_2 contents (1.08–1.43 wt%), and no correlation exists between Nb/Ta vs. TiO_2 (Fig. 7d and inset). We thus infer that the negative Nb—Ta anomalies of the Ailaoshan hornblende diorites may reflect the magma source characteristics. Accessory minerals, such as zircon, apatite, allanite and monazite, strongly influence the trace elements compositions of igneous rocks. Removal of zircon and apatite would decrease Zr and P_2O_5 contents, whereas the Ailaoshan hornblende diorites show no negative Zr and P_2O_5 vs. SiO_2 correlations (Fig. 7e and f). Allanite and monazite are LREE-enriched, and minor fractionation of them would lead to marked LREE depletion, which is absent in the Ailaoshan hornblende diorites ($(La/Yb)_N = 3.09–3.45$). Therefore, we infer that the Ailaoshan hornblende diorites have experienced insignificant fractionation of accessory minerals (e.g., zircon, apatite, allanite and monazite).

5.1.2. Magma source and mantle-crust interaction

Experimental studies suggest that partial melts from basaltic lower crust rocks tend to have low Mg# (<40) regardless of the melting degree (Fig. 4d) (Rapp and Watson, 1995). Recent study by Wang et al. (2018) suggested that the Late Archean diorites with high Mg# (49–52) were probably derived from partial melting of the lower crust. However, the Late Archean diorites they reported have significantly higher SiO_2

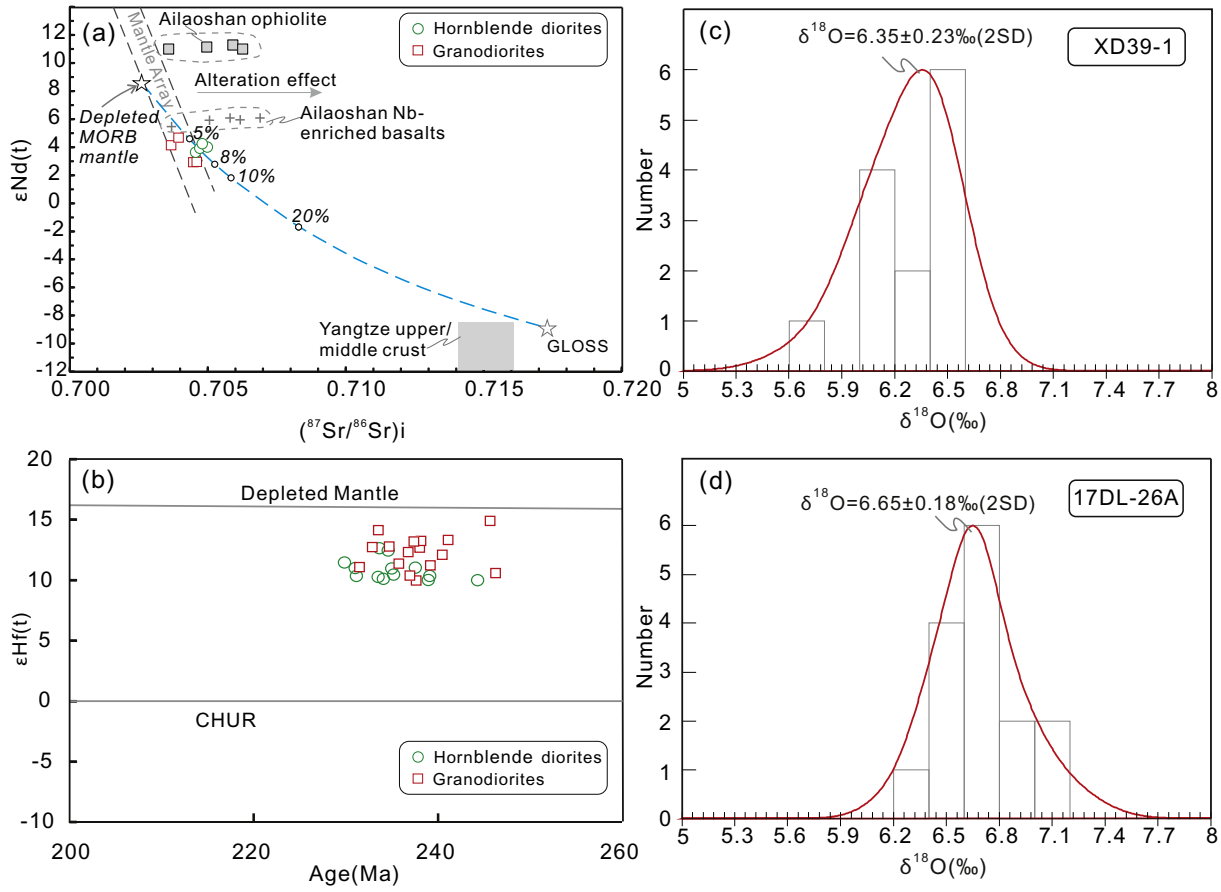

Fig. 6. (a) εNd(t) versus $(^{87}Sr/^{86}Sr)_i$ diagram. Dashed line shows that the mantle source of the Ailaoshan hornblende diorites may have been a binary mixture between the depleted mid-ocean ridge basalt (MORB) mantle and ~5% subducted oceanic sediment-derived melts. See Supplementary Table S5 for detail of the mixing model. (b) Plots of εHf(t) versus U—Pb ages of zircon grains. Oxygen isotopic compositions of zircon grains from hornblende diorites (c) and granodiorites (d). Data sources: depleted MORB mantle ($(^{87}Sr/^{86}Sr)_i = 0.702601$; εNd(t) = +8.61) are from Gale et al. (2013); Global oceanic sediments (GLOSS) ($(^{87}Sr/^{86}Sr)_i = 0.715594$; εNd (t) = −8.9) are from Plank and Langmuir (1998); Ailaoshan ophiolites are from Xu and Castillo (2004); Ailaoshan Nb-enriched basalts are from Xu et al. (2019c).

contents (59–66 wt%) than the Ailaoshao hornblende diorites. The Ailaoshan hornblende diorites are characterized by low SiO_2 contents (50–54 wt%, average 52 wt%) and high Mg# (48–57, average 53), suggesting that they were most likely derived from the mantle instead of crustal rocks, which are generally more felsic (SiO_2 = 50–63 wt%; Rudnick and Gao, 2003).

The hornblende diorites are characterized by LILE enrichments and HFSE depletions (Fig. 5b), which may indicate either crustal contamination or source enrichment (e.g., by recycled terrigenous sediments or subduction zone fluid), or a combination of both. Inherited zircon grains are absent in the hornblende diorites according to cathodoluminescence (CL) imaging and U—Pb dating results (Fig. 3a; Supplementary Table S1). The hornblende diorites do not show clear increasing $(^{87}Sr/^{86}Sr)_i$ trend with SiO_2 or 1/Sr*10000, or decreasing Nd (t) trend with increasing SiO_2 (or decreasing Nb/La) (Figs. 8a-d), thus showing no major crustal contamination (Guo et al., 2016; Liu et al., 2017b). In addition, the hornblende diorites show narrow ranges of $(^{87}Sr/^{86}Sr)_i$ (0.7046–0.7050), εNd(t) (+3.63 to +4.22) and $\varepsilon Hf(t)_{zircon}$ (+9.9 to +12.6), suggesting that crustal contamination was insignificant in the magmatic evolution. Therefore, we infer that parental magma of the hornblende diorites was derived from the depleted mantle wedge metasomatized by subduction-related melts and/or fluids.

In subduction zones, slab-derived fluids tend to be more enriched in LILEs than REEs and HFSEs, making Ba/La and Ba/Nb ideal tracers for slab fluids (Guo et al., 2016; Hanyu et al., 2006). In contrast, Ba, La and Nb are high incompatible during melting of the subducted sediments, hence Ba/Nb and Ba/La ratios of the sediment-derived melt would be similar to the subducted sediments (e.g., Guo et al., 2016). Subducted sediment-derived melts are characterized by high contents of Th, LREE and high Th/La ratio (Plank et al., 2007). Most of the hornblende diorites have relatively high contents of Th (5.52–8.40 ppm), high Th/La (0.45–0.66) and Th/Yb (2.01–3.20) ratios, but low Ba/Nb (66–94) and Ba/La (19–27) ratios. Previous studies have shown that variable degrees of crystal accumulation may exert a significant influence on the trace element abundance and elemental ratios (e.g., Th/REE, Th/HFSE, Ba/REE and Ba/HFSE ratios; Guo et al., 2016). Guo et al. (2016) have evaluated the feasibility of using Th/La, Th/Yb, Ba/La and Ba/Nb ratios to tracking the sediment/fluid input into a mantle wedge. Their results suggest that minor fractional crystallization of the Th-rich accessory minerals such as zircon, monazite and apatite would greatly affect Th/La and Th/Yb ratios of parental magmas, which may give rise to the relatively high Th/La and Th/Yb ratios of Ailaoshan hornblende diorites. Therefore, to avoid overestimating the content of sediment flux (melt and/or fluid), we used Ba/La and Ba/Nb ratios to investigate the enrichment process beneath the sub-arc mantle in this study. Our trace element modeling results indicate that adding ~5% sediments into the depleted mantle wedge could reproduce the Ba/Nb, Ba/La ratios and εNd(t) of the Ailaoshan hornblende diorites (Fig. 9a and b). This suggests that the subduction-related sediments (rather than fluids) may have contributed to the source enrichment.

The Nd—Hf isotope compositions of the hornblende diorites are plotted on the island arc array (Fig. 10a) (Chauvel et al., 2008). Previous studies argued that the slope of the array may have resulted from Nd—Hf decoupling during the dehydration and/or melting of the

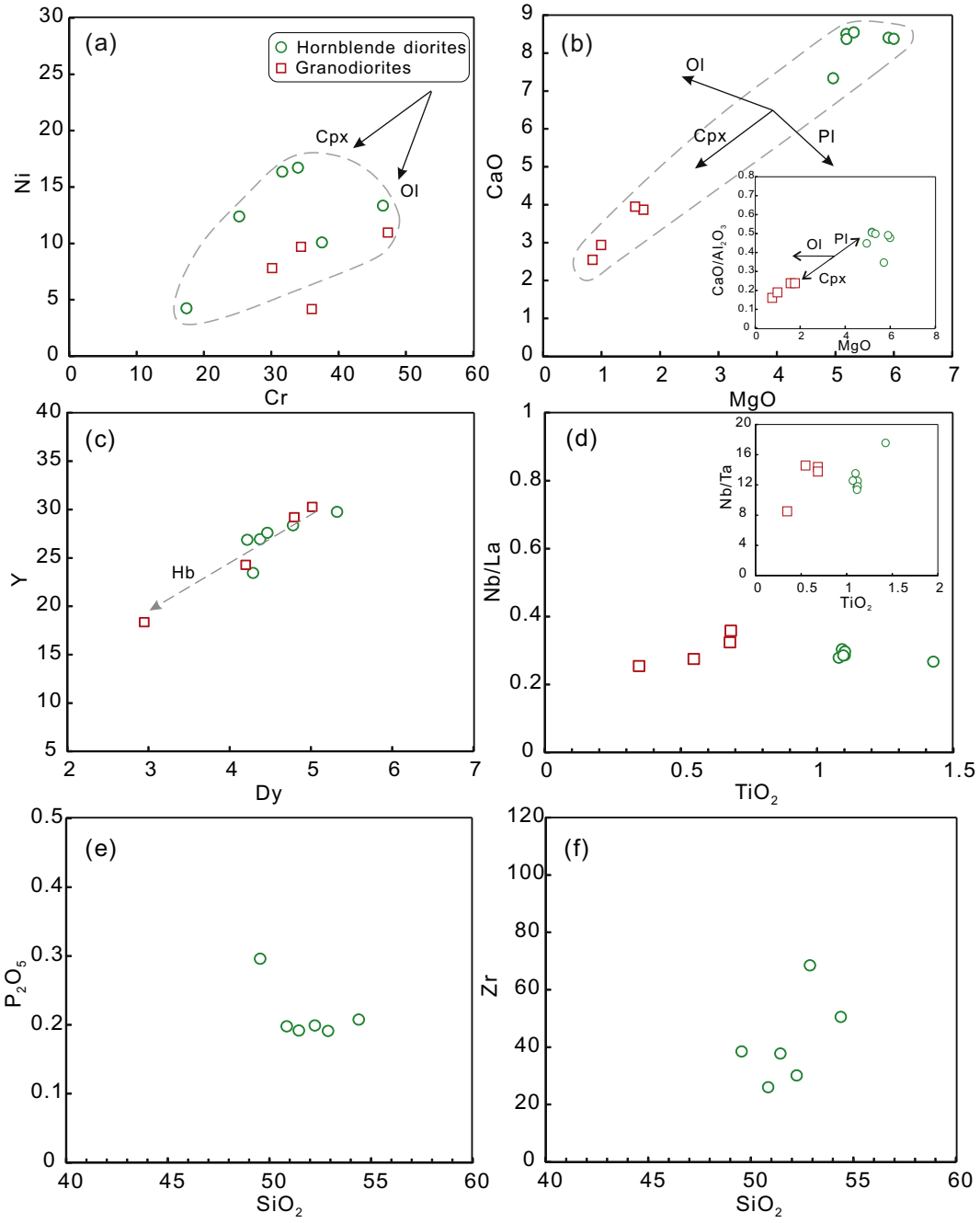

Fig. 7. Binary diagrams of (a) Ni versus Cr, (b) CaO and CaO/Al_2O_3 (b inset) versus MgO, (c) Y versus Dy, (d) Nb/La and Nb/Ta (d inset) versus TiO_2, (e) P_2O_5 versus SiO_2 and (f) Zr versus SiO_2 for Ailaoshan hornblende diorites and granodiorites. Mineral abbreviations: Cpx = clinopyroxene; Hb = Hornblende.

subducted slab, with a sedimentary component characterized by elevated Nd/Hf ratios (Tollstrup and Gill, 2005). Because Nd is more mobile than Hf in hydrothermal fluids, the Nd isotopic compositions are likely more affected by subduction-related metasomatism (Kogiso et al., 1997). Non-radiogenic Nd tends to be transported into the mantle wedge by the slab-derived fluids, which lower the magma Nd isotope ratios. In contrast, the Hf isotope ratios of the metasomatized mantle wedge would not be significantly modified (Hanyu et al., 2006). As above-mentioned, our data indicate that the subducted sediments played a major role in shaping the geochemical characters of the arc-type hornblende diorites from the Ailaoshan metamorphic complex, and we suggest that the island arc Nd—Hf isotope trend could be mainly controlled by the mixing of depleted mantle and subducted sediments (Chauvel et al., 2008).

We conducted Sr-Nd-Hf isotope modeling using the average MORB (Chauvel et al., 2008; Su, 2002) as the mantle end-member and global subducting sediments (GLOSS) as the crustal end-member (Plank and Langmuir, 1998). Our modeling indicates that adding 5% sediment-derived melts into the mantle wedge could reproduce the Sr-Nd-Hf isotope compositions of the hornblende diorites (Figs. 6a and 10). The Ailaoshan hornblende diorites have clearly higher $\delta^{18}O_{zircon}$ values (5.8–6.6‰, mean 6.35 ± 0.23‰; Fig. 6c) than the zircon in equilibrium with typical mantle-derived magmas (5.3 ± 0.3‰, 1σ) (Valley et al., 2005). Although partial melting of metavolcanic rocks modified by low-temperature alteration may also yield elevated $\delta^{18}O$ values (e.g., Wang et al., 2018), this is unlikely as the Ailaoshan hornblende diorites are probably derived from partial melting of the metasomatized mantle rather than the lower crust as above-discussed. Therefore, the

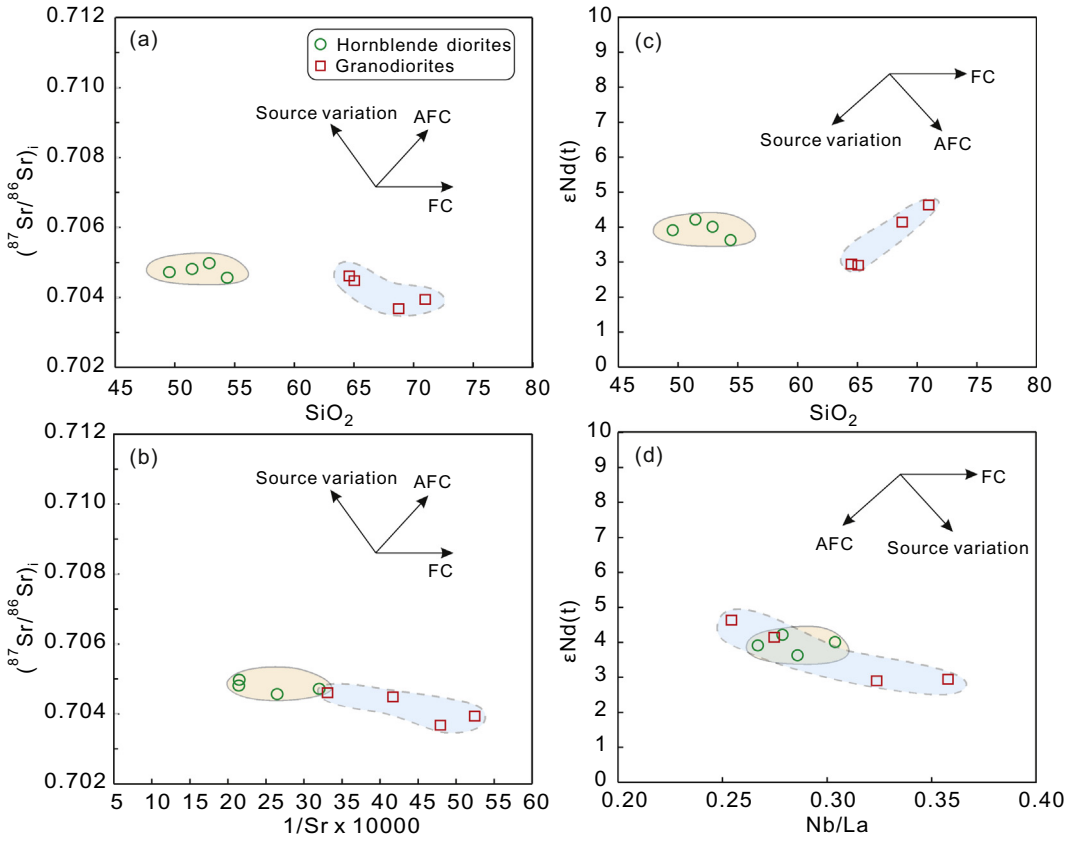

Fig. 8. (a) $(^{87}Sr/^{86}Sr)i$ versus SiO_2, (b) $(^{87}Sr/^{86}Sr)i$ versus 1/Sr × 10,000, (c) εNd(t) versus SiO_2, and (d) εNd(t) versus Nb/La diagrams for the Ailaoshan hornblende diorites and granodiorites.

elevated $\delta^{18}O$ values of these rocks are mainly resulted from the ^{18}O-rich supracrustal input in the subduction zone (e.g., subducting sediment-derived melts). The Hf—O isotopic mixing model shows that input from such a high-$\delta^{18}O$ (ca. 20‰) subducting sediment end-member is required to generate the hornblende diorites (Fig. 11a and b). GLOSS is dominated by terrigenous material (ca. 76 wt%) and minor calcium carbonate (ca. 7 wt%) (Plank and Langmuir, 1998), which both have high $\delta^{18}O$ values (10‰ to 30‰; Valley et al., 2005). Therefore, we infer that high-$\delta^{18}O$ GLOSS was involved in melt generation during the subduction of the Ailaoshan Ocean.

The flat HREE patterns (Fig. 5a) of the hornblende diorites suggest that the partial melting most likely occurred in spinel-facies mantle or at a relatively shallow depth (McKenzie and O'Nions, 1991), and the garnet may have not been an important residual phase. We therefore select spinel peridotite to model nonmodal batch melting, which is common in the generation of mantle-derived magmas. The partition coefficient used in such mantle melting are from Kelemen et al. (2003) and Pilet et al. (2011). The trace element partial melting modeling results further support that the hornblende diorites could be generated by 10% melting of depleted mantle metasomatized by ~5% subducted sediments (Fig. 12).

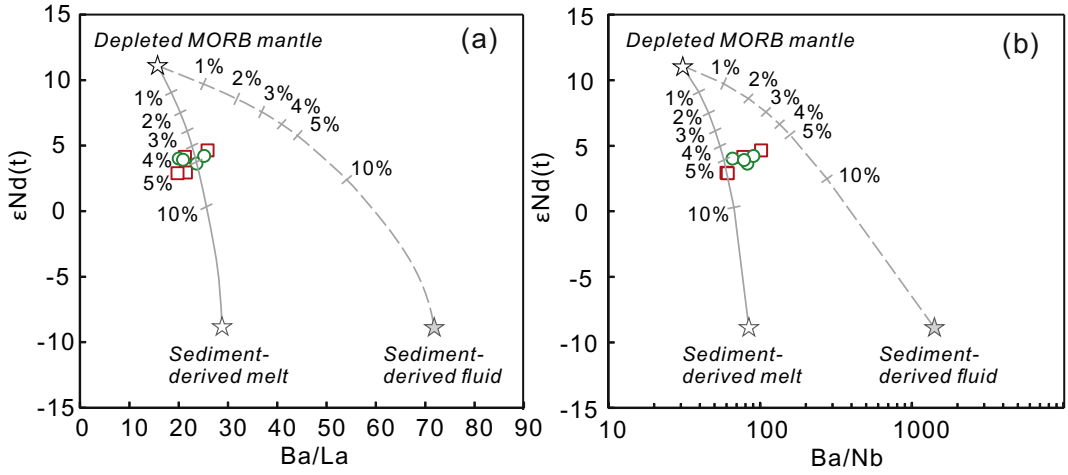

Fig. 9. (a) Plot of εNd(t) versus Ba/La, and (b) plot of εNd(t) versus Ba/Nd for the Middle Triassic Ailaoshan hornblende diorites and granodiorites. See Supplementary Table S6 for detail of the mixing and melting model as well as different end-member compositions on the mixing lines. Data for subducted sediments are from Plank and Langmuir (1998).

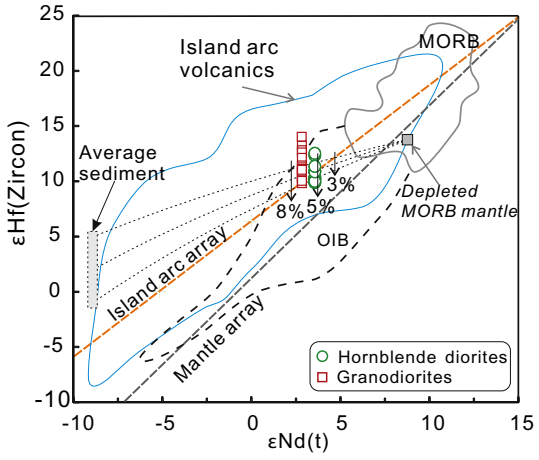

Fig. 10. $\varepsilon Hf_{(zircon)}$ versus εNd(t) diagrams for the hornblende diorites and granodiorites. Data sources: GLOSS (global oceanic sediments) with average εNd (−8) and εHf (+2 ± 3) values from Plank and Langmuir (1998); Island arc lavas, ocean island basalt (OIB), mid-ocean ridge basalt (MORB), depleted MORB mantle (εNd(t) = +8.8; εHf = +13.9), island arc array (εHf = 1.23 × εNd + 3.36) and mantle array (εHf = 1.59 × εNd + 1.28) are from Su et al. (2002) and Chauvel et al. (2008). See Supplementary Table S5 for detail of the mixing model.

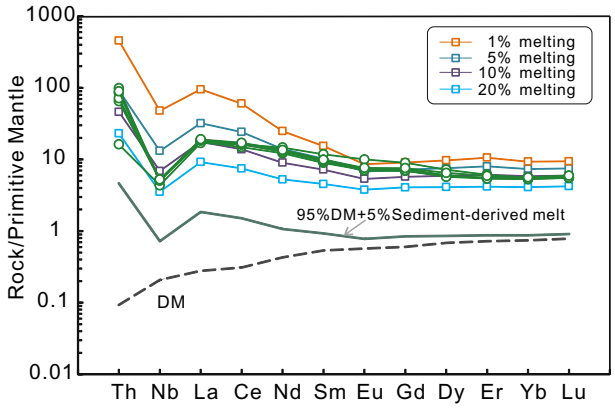

Fig. 12. Trace-element modeling results for nonmodal batch melting of spinel peridotite. The depleted mantle (DM, dashed line; Workman and Hart, 2005) mixed with ~5% subducted sediments to produce the metasomatized mantle wedge source (solid line) of the Ailaoshan hornblende diroites. See Supplementary Table S7 for details of the mixing and melting model as well as different end-member compositions on the mixing lines.

5.2. Petrogenesis of the granodiorites

Both the granodiorites and hornblende diorites intruded into the Ailaoshan Group in the metamorphic complex, have similar age and Sr-Nd-Hf-O isotope compositions (Figs. 3 and 6), and fall onto the same fractionation trend (Figs. 13a–f), suggesting that the two rock types were comagmatic. Compared to the hornblende diorites, the granodiorites contain higher SiO_2 and lower Mg# values, Al_2O_3, MgO, Fe_2OT 3, and CaO contents. Both rock types show similar LILE enrichments and HFSE depletions in the primitive mantle-normalized multi-elements (Fig. 5b and d), although the more fractionated granodiorites contain higher incompatible trace element components. This indicates that the granodiorites were probably formed from fractional crystallization of mafic magmas. The granodiorites show positive Cr vs. Ni and MgO vs. CaO (CaO/Al_2O_3) correlations (Fig. 7a and b), indicating clinopyroxene fractionation. The positive Dy vs. Yb correlation indicates hornblende fractionation (Fig. 7c). The negative Eu anomalies (Eu/Eu* = 0.81–0.84), and the positive Sr/Y vs. Eu/Eu* correlation indicate plagioclase fractionation (Figs. 14a). The negative total REE vs. Eu/Eu*, Rb vs. Sr and Ba vs. Sr correlations may suggest a combined fractionation of hornblende, clinopyroxene and plagioclase (Fig. 14b, c and d). Using the hornblende diorite sample 17DL-26B (which has the lowest total REE and SiO_2 contents) as the initial melts and the partition coefficients from McKenzie and O'Nions (1991), Rayleigh fractionation modeling (40% hornblende +30% clinopyroxene +30% plagioclase) successfully reproduced the trace element variations of the Ailaoshan hornblende diorites and granodiorites (Figs. 14b-d). This further supports that the granodiorites were formed via fractionation crystallization of the mafic magmas.

Fractional crystallization of silicate magmas should produce a continuum of mafic to felsic composition (Singer et al., 1992), yet a compositional or silica gap (i.e., Daly Gap) is observed between the hornblende diorites and the granodiorites (Fig. 13). We interpreted this "Daly Gap" to be caused by extensive Fe-oxide mineral fractionation (e.g., magnetite) (Shellnutt et al., 2009). The granodiorites display positive FeO^T vs. TiO_2 correlation, consistent with the Fe—Ti oxide fractionation. Formation of the Daly Gap through fractional crystallization has been documented in many other calc-alkaline magmatic systems (e.g., Aleutian calc-alkaline volcanic centers) (Brophy, 1991).

Compared to the hornblende diorite, the granodiorite has a little higher initial $^{87}Sr/^{86}Sr$ values (Fig. 8). This could be explained by that the granodiorite was formed by fractional crystallization of mafic magma that similar (but not exactly identical) to the hornblende

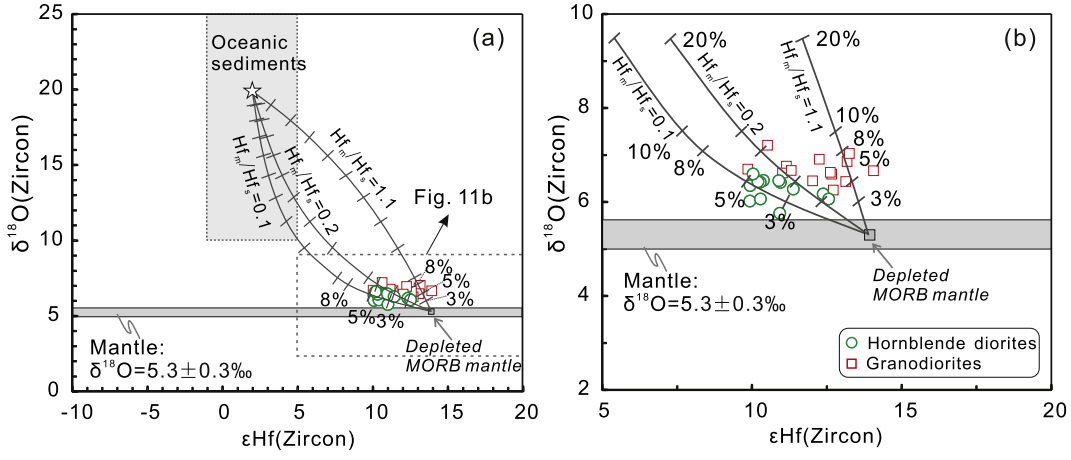

Fig. 11. (a–b) $\delta^{18}O_{(zircon)}$ versus $\varepsilon Hf_{(zircon)}$ diagrams for the hornblende diorites and granodiorites. Data sources: $\delta^{18}O_{(zircon)}$ from mantle-derived magmas (5.3 ± 0.3‰, 1σ) and oceanic sediments (10–25‰) are from Valley et al. (1998, 2005).

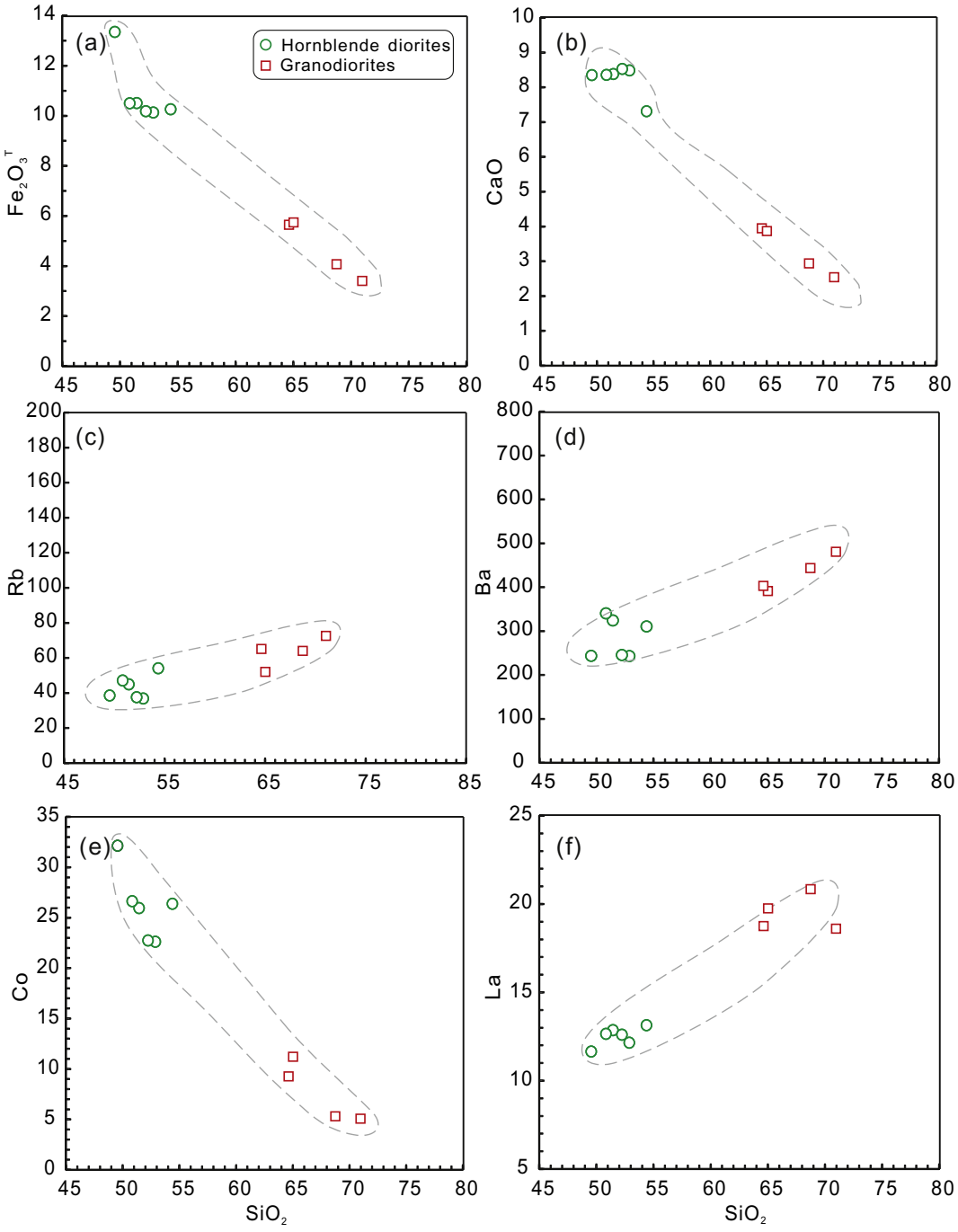

Fig. 13. Hacker diagrams of the selected major and trace elements for the Ailaoshan hornblende diorites and granodiorites: (a) Fe_2OT 3 versus SiO_2; (b) CaO versus SiO_2; (c) Rb versus SiO_2; (d) Ba versus SiO_2; (e) Co versus SiO_2; (f) La versus SiO_2.

diorites. Such kind of parental mafic magma may have relatively variable Sr isotopic compositions.

5.3. Geodynamic implications

West-dipping subduction of the east Paleotethys Jinshajiang-Ailaoshan-Song Ma branch beneath the Indochina Block is widely accepted due to the well-preserved Permian-Triassic arc-type magmas extending from Jomda-Weixi in the north through Taizhong-Lixianjiang to Truong Son in the south (e.g., Liu et al., 2012; Wei and Shen, 1997). For example, extensive Permian-Triassic arc-type magmatism were reported in the western Ailaoshan volcanic belts (Lai et al., 2014a; Liu et al., 2011; Liu et al., 2017b; Wei and Shen, 1997), Such as the arc/back-arc-type Wusu-Yaxuanqiao-Maoheshan basaltic rocks (287–248 Ma) and Dalongkai ultramafic-mafic intrusions (272–266 Ma), which were interpreted to be originated from a MORB-like mantle source metasomatized by subduction-related fluids or sediments (Fan et al., 2010; Liu et al., 2011; Liu et al., 2017b). However, hypotheses on east-dipping subduction remain controversial, mainly because of the absence of Permian-Triassic continental island arc rocks in SW China, and the structural overprinting of the Cenozoic India-Asia collision. Our recent studies on the Late Permian Nb-enriched basalts (NEBs) in the Ailaoshan metamorphic complex suggested that they were generated by mixing between the depleted MORB-derived

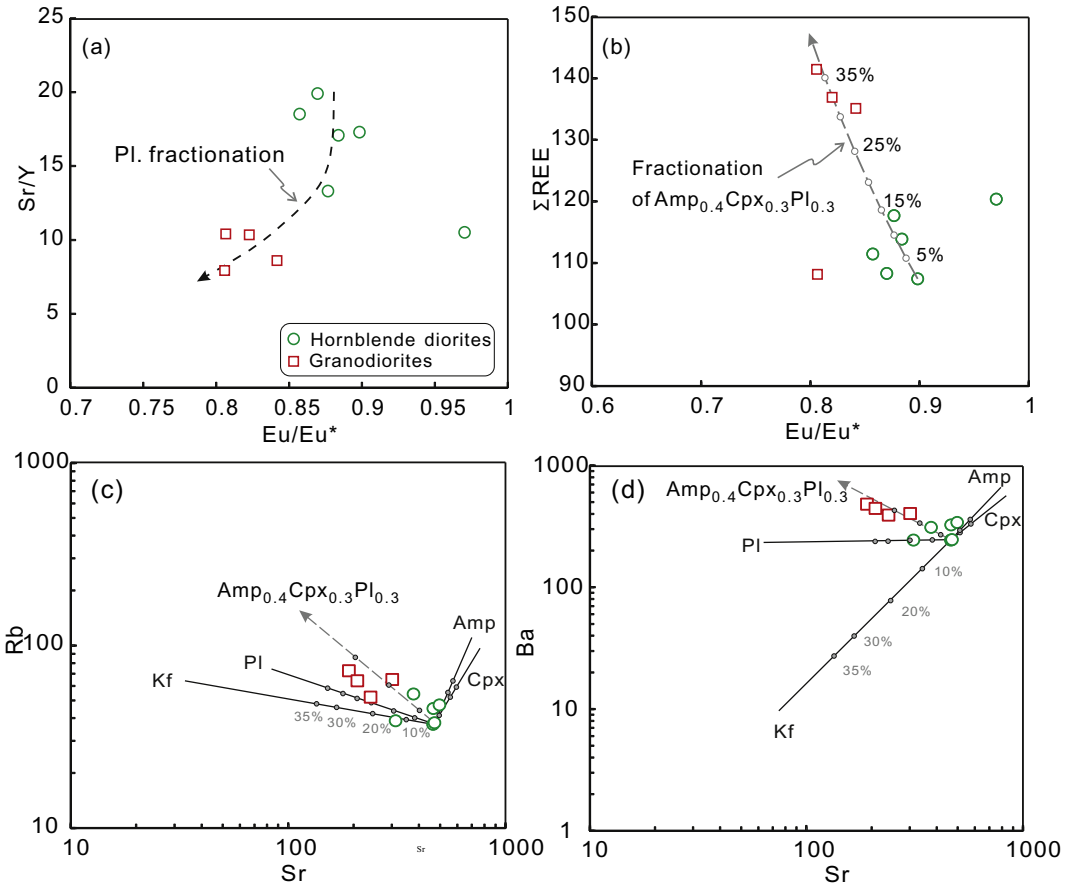

Fig. 14. (a) Sr/Y versus Eu/Eu* and (b) ΣREE (total rare earth element) versus Eu/Eu* diagrams, showing trends of fractional crystallization. The sample 17DL-26B is assumed as the initial melts before Rayleigh fractionation (40% hornblende +30% clinopyroxene +30% plagioclase). The numbers of the curves denote the degrees of fractional crystallization in percent, using the partition coefficients of McKenzie and O'Nions (1991).

and enriched mantle-derived components, and were probably the products of the interaction between the eastward subduction of the Paleotethyan Ailaoshan Ocean and the near-by Emeishan mantle plume (Xu et al., 2019c). We thus infer that the eastward subduction of the Ailaoshan Ocean could exist in the Permian.

Geochemical and Sr-Nd-Hf-O isotopic compositions of the Middle Triassic (ca. 235–237 Ma) hornblende diorites and the granodiorites show typical arc-type geochemical affinities. Petrogenesis analyses mentioned above indicate their derivations from partial melting of the mantle wedge metasomatized by subducted oceanic sediments, and subsequent magma fractionation. The intrusion contact between the Ailaoshan Group and hornblende diorite/granodiorite is observed in the field. Therefore, we considered that these rocks represent remnants of an arc developed in the western margin of the South China Block, and that bipolar subduction was responsible for the closure of the Ailaoshan Ocean.

Due to extensive tectonic overprinting of pre-Late Triassic top-to-the-NE ductile shearing and post-Late Triassic left-lateral ductile shearing (Faure et al., 2016a), both commonly well developed in the Ailaoshan belt, the hornblende diorites and granodiorites can be alternatively attributed to be exotic tectonic blocks/lenses in the Ailaoshan metamorphic complex, or be the product of westward subduction of the Ailaoshan Ocean beneath the Indochina-Simao Block, similar to that in the Taizhong-Lixianjiang Arc belt. However, we consider that unlikely based on the data presented in this and previous studies: Zircon εHf(t) values for the studied rocks here are mainly positive, in contrast to those of the Taizhong-Lixianjiang arc rocks, such as the Xin'anzhai granitoids (εHf(t) = −6.2 to −9.8; Liu et al., 2015). Previous detrital zircon evidence also suggests that no pre-Late Triassic sequence deposited west of the suture were transported to the east by later tectonic movements (Wang et al., 2014; Xia et al., 2019; Xu et al., 2019a).

Our explanation above is also consistent with our previous detrital zircon results on the Permian-Triassic sedimentary sequences across the Ailaoshan belt (Xia et al., 2019; Xu et al., 2019a, 2019b). The Permian-Middle Triassic sequences in the both western South China margin and eastern Indochina showed unimodal detrital zircon age population of 280–237 Ma and 273–236 Ma, respectively (Xia et al., 2019; Xu et al., 2019a). The unimodal detrital zircon age patterns indicate arc-related depositional environment (e.g., fore-arc basin) and the development of two distinct Permian-Triassic continental arc systems in both the eastern Indochina (i.e., Taizhong-Lixianjiang arc) and the western South China (central and west Yunnan) (Xia et al., 2019; Xu et al., 2019a). However, there is no any report on the arc rocks developed in the western South China up to now. Our present study provides the first direct evidence for this arc in the Ailaoshan fold belt.

In contrast, the Upper Triassic sedimentary sequences on both sides of the Ailaoshan suture show multiple but similar detrital zircon age spectra and Hf isotopic compositions, which indicates that the Upper Triassic sedimentary sequences could be deposited in a foreland basin, and the Ailaoshan Ocean was likely closed between the late Middle Triassic-early Late Triassic (Xu et al., 2019a). Our recent geochemical studies on the Permian-Triassic sedimentary rocks in the eastern Indochina Block also revealed a dramatic provenance change from continental arc to mature orogenic belt source across the Middle-Upper Triassic boundary, implied a late Middle Triassic-early Late Triassic closure of the Ailaoshan Ocean (Xu et al., 2019b). This inference is consistent

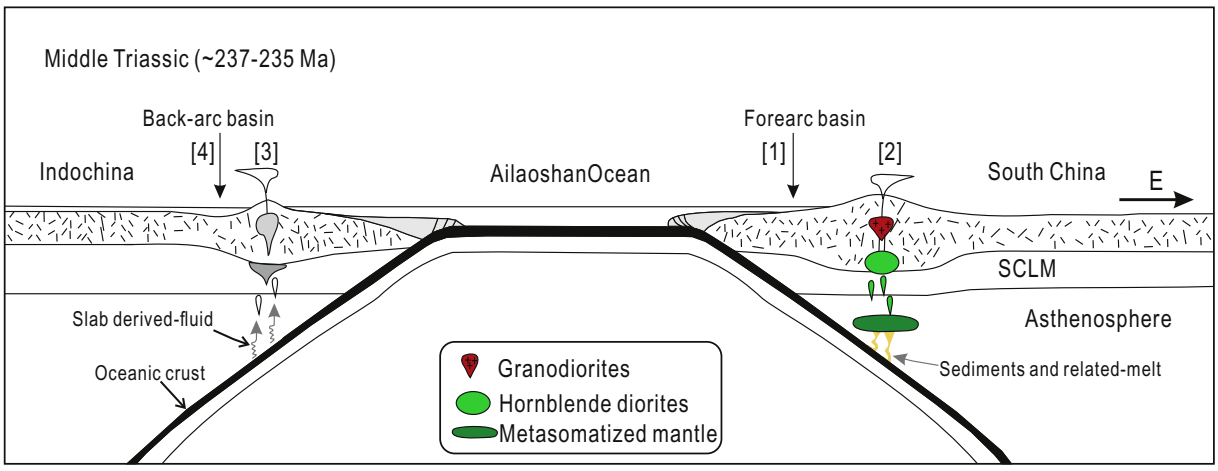

Fig. 15. Schematic diagram illustrating a bipolar subduction of the Ailaoshan Ocean and the formation of the Ailaoshan arc-type hornblende diorites and granodiorites during the Middle Triassic. Middle Triassic forearc basin received detritus eroded from the Permian-Triassic arc system in the South China western margin ([1], e.g., Xia et al., 2019; Xu et al., 2019a). Remnants of the Permian-Triassic arc ([2], this study). Permian-Triassic Taizhong-Lixianjiang arc in the eastern Indochina ([3], e.g., Fan et al., 2010; Lai et al., 2014a; Liu et al., 2017b; Liu et al., 2011). Back-arc basin received detritus derived from the Permian-Triassic Taizhong-Lixianjiang arc ([4], e.g., Xia et al., 2019; Xu et al., 2019a, 2019b).

with the observation of the Upper Triassic red conglomerate and sandstone (molasse) unconformably covering the Early-Middle Triassic or the late Paleozoic sequences across the Ailaoshan belt (Faure et al., 2016a). These results are also consistent with abundant magmatic, paleomagnetic and metamorphic evidence, which also supports a late Middle Triassic to early Late Triassic closure of the Ailaoshan Ocean (e.g., Lai et al., 2014a; Zhang et al., 2014b). The collision time between the South China and Indochina in central-northern Vietnam was suggested to be a little earlier, around late Early Triassic to early Middle Triassic (Faure et al., 2014), and thus the closure of the Ailaoshan-Song Ma Ocean was likely to be diachronous (Cai and Zhang, 2009; Lai et al., 2014a). The early Late Triassic collision-related granitoids in Jinshajiang (ca. 235–230 Ma; Zhu et al., 2011)-Ailaoshan (ca. 229 Ma; Liu et al., 2014) region also suggested that the Ailaoshan Ocean was likely completely closed by the Late Triassic. Moreover, post-collisional granitoids commonly have sizeable proportion of inherited zircons, such as the crust-derived granites of the Variscan French Massif Central (e.g., Moyen et al., 2017), whereas no inherited zircons were found from the Ailaoshan hornblende diorites and granodiorites. Therefore, the arc-type geochemical characters of our Middle Triassic (237–235 Ma) hornblende diorites and granodiorites are most likely derived from the metasomatized mantle wedge rather than from remelting of the juvenile crustal materials as the Late Triassic (ca. 229 Ma) Huashiban I-type granites (e.g., Liu et al., 2014).

Previous studies focused on the Permian-Triassic igneous and sedimentary rocks in the South China Block may also suggest the eastward subduction of the eastern Paleotethys branch ocean (Hou et al., 2017; Ke et al., 2018; Lepvrier et al., 2004; Li et al., 2006b; Qin et al., 2011, 2012; Wang et al., 2013; Zhang et al., 2014b). For examples, a series of Triassic volcanic outcrops, such as the Middle Triassic (ca. 250–246 Ma) felsic (e.g., dacite and rhyolite) and mafic (e.g., basalt) volcanic rocks, have been reported in SW Guangxi (SW China) (Qin et al., 2011, 2012). The SW Guangxi dacite and rhyolite share geochemical similarity to the typical subduction-related arc volcanic rocks (Qin et al., 2011). Qin et al. (2012) divided the basalts into three geochemical groups: back-arc basin (Group 1), island arc (Group 2) and ocean island basalts (OIB) (Group 3). The Middle Triassic felsic volcanics and their mafic counterparts may imply an arc—/back arc-basin system developed along the border of SW Guangxi, which could be resulted from the eastward subduction of the Indochina Block beneath the South China Block (Qin et al., 2011, 2012). In Junying-Bangxi area (Hainan Island, South China), a Middle Permian (ca. 269 Ma) OIB-like ultramafic-mafic lava suite was recognized (Wang et al., 2013), and was interpreted to have formed in a back-arc basin owing to the eastward subduction of Paleo-Tethys ocean (Wang et al., 2013). In northern Vietnam, eastward Paleotethyan subduction was also proposed by some authors (Lepvrier et al., 2004; Zhang et al., 2014).

Thus, our new results, combined with previous studies in the whole Ailaoshan tectonic zone and its adjacent regions in the South China Block (e.g., SW Guangxi and Hainan Island), consistently indicate that eastward subduction of the Ailaoshan Ocean beneath the South China Block did occur, and the Ailaoshan Ocean has not been completely closed before the late Middle Triassic. We therefore propose that the Middle Triassic Paleotethyan Ailaoshan Ocean may have been bipolar-subducted both westward and eastward beneath the Indochina and South China blocks, respectively (Fig. 15). The newly identified two rock types likely represent remnants of a continental arc, and may have supplied the detritus for the Permian-Triassic sedimentary basins in the western South China continental margin, although older (Permian-Early Triassic) arc-type magmatic rocks in the Ailaoshan metamorphic complex may have been eroded or yet to be discovered.

6. Conclusions

(1) The first identified Middle Triassic (ca. 235–237 Ma) hornblende diorites and granodiorites in the Ailaoshan high-grade metamorphic complex show typical arc affinities, and were likely sourced from the depleted mantle metasomatized by subducted oceanic sediments.
(2) The hornblende diorite-granodiorite could be remnants of the Permian-Triassic arc root in the western South China margin.
(3) Identification of remnants of this Middle Triassic island arc supports east-dipping subduction of the Ailaoshan Ocean. We propose that the Paleotethyan Ailaoshan Ocean may have been bipolar-subducted both westward and eastward beneath the Indochina and South China blocks, respectively.

Declaration of Competing Interest

The authors declare that they have no known competing financial interests or personal relationships that could have appeared to influence the work reported in this paper.

Acknowledgments

We acknowledge the constructive reviews and comments of Faure Michel and another anonymous reviewer and Editor Xian-Hua Li. This work was financially supported by the Second Tibetan Plateau Scientific

Expedition and Research (STEP) (2019QZKK0702), the National Key R & D Program of China (2016YFC0600407) to Prof. Xiao-Ping Xia. We appreciate the assistance of Wen Zeng and Sheng-Ling Sun with whole rock trace element and Sr—Nd isotope analyses. This is contribution NO. IS-2822 from GIGCAS. Presented data can be obtained in the Supplementary Tables S1-S7 in the Supplementary Material.

Appendix A. Supplementary data

Supplementary data to this article can be found online at https://doi.org/10.1016/j.lithos.2020.105447.

References

Brophy, J.G., 1991. Composition gaps, critical crystallinity, and fractional crystallization in orogenic (calc-alkaline) magmatic systems. Contrib. Mineral. Petrol. 109 (2), 173–182.
Cai, J.-X., Zhang, K.-J., 2009. A new model for the Indochina and South China collision during the late Permian to the Middle Triassic. Tectonophysics 467, 35–43.
Chauvel, C., Lewin, E., Carpentier, M., Arndt, N.T., Marini, J.-C., 2008. Role of recycled oceanic basalt and sediment in generating the Hf–Nd mantle array. Nat. Geosci. 1, 64–67.
Chung, S.-L., Lee, T.-Y., Lo, C.-H., Wang, P.-L., Chen, C.-Y., Yem, N.T., Hoa, T.T., Genyao, W., 1997. Intraplate extension prior to continental extrusion along the Ailao Shan-Red River shear zone. Geology 25, 311–314.
Corfu, F., Hanchar, J.M., Hoskin, P.W., Kinny, P., 2003. Atlas of zircon textures. Rev. Mineral. Geochem. 53, 469–500.
Fan, W., Yuejun, W., Aimei, Z., Feifei, Z., Yuzhi, Z., 2010. Permian arc-back-arc basin development along the Ailaoshan tectonic zone: Geochemical, isotopic and geochronological evidence from the Mojiang volcanic rocks, Southwest China. Lithos 119, 553–568.
Faure, M., Lepvrier, C., Nguyen, V.V., Vu, T.V., Lin, W., Chen, Z., 2014. The South China block-Indochina collision: where, when, and how? J. Asian Earth Sci. 79, 260–274.
Faure, M., Lin, W., Chu, Y., Lepvrier, C., 2016a. Triassic tectonics of the Ailaoshan Belt (SW China): early Triassic collision between the South China and Indochina Blocks, and Middle Triassic intracontinental shearing. Tectonophysics 683, 27–42.
Faure, M., Lin, W., Chu, Y., Lepvrier, C., 2016b. Triassic tectonics of the southern margin of the South China Block. C. R. Geosci. 348 (1), 5–14.
Faure, M., Hoai, L.T.T., Lepvrier, C., 2018. Early Paleozoic or Early-Middle Triassic collision between the South China and Indochina blocks: the controversy resolved? Structural insights from the Kon Tum massif (Central Vietnam). J. Asian Earth Sci. 166, 162–180.
Gale, A., Dalton, C.A., Langmuir, C.H., Su, Y., Schilling, J.-G., 2013. The mean composition of ocean ridge basalts. Geochem. Geophys. Geosyst. 14, 489–518.
Guo, F., Li, H., Fan, W., Li, J., Zhao, L., Huang, M., 2016. Variable sediment flux in generation of Permian subduction-related mafic intrusions from the Yanbian region, NE China. Lithos 261, 195–215.
Hanyu, T., Tatsumi, Y., Nakai, S., Chang, Q., Miyazaki, T., Sato, K., Tani, K., Shibata, T., Yoshida, T., 2006. Contribution of slab melting and slab dehydration to magmatism in the NE Japan arc for the last 25 Myr: Constraints from geochemistry. Geochem. Geophys. Geosyst. 7, 1–29.
Hawkesworth, C.J., Gallagher, K., And, J.M.H., Mcdermott, F., 1993. Mantle and Slab Contributions in ARC Magmas. Annu. Rev. Earth Planet. Sci. 21, 175–204.
Hou, Y.-L., Zhong, Y.-T., Xu, Y.-G., He, B., 2017. The provenance of late Permian karstic bauxite deposits in SW China, constrained by the geochemistry of interbedded clastic rocks, and U–Pb–Hf–O isotopes of detrital zircons. Lithos 278-281, 240–254.
Ji, L., Liu, F., Wang, F., Santosh, M., Tian, Z., Sun, Z., Tang, L., 2020. Mineral phase equilibria and zircon geochronology constrain multiple metamorphic events of high-pressure pelitic granulites in south-eastern Tibetan Plateau. Geol. J. 55 (2), 1332–1356.
Ke, X., Zhang, Z., Yang, J., Yao, H., Zhu, L., He, W., 2018. Radiolarian and detrital zircon in the Upper Carboniferous to Permian Bancheng Formation, Qinfang Basin, and the geological significance. J. Earth Sci. 29, 594–606.
Kelemen, P.B., Yogodzinski, G.M., Scholl, D.W., 2003. Along-strike variation in the Aleutian Island Arc: Genesis of high Mg# andesite and implications for continental crust. Inside Subduction Fact. 138, 223–276.
Kogiso, T., Tatsumi, Y., Nakano, S., 1997. Trace element transport during dehydration processes in the subducted oceanic crust: 1. Experiments and implications for the origin of ocean island basalts. Earth Planet. Sci. Lett. 148, 193–205.
Lai, C.K., Meffre, S., Crawford, A.J., Zaw, K., Xue, C.D., Halpin, J.A., 2014a. The Western Ailaoshan Volcanic Belts and their SE Asia connection: a new tectonic model for the Eastern Indochina Block. Gondw. Res. 26, 52–74.
Lai, C.K., Meffre, S., Crawford, A.J., Zaw, K., Halpin, J.A., Xue, C.D., Salam, A., 2014b. The Central Ailaoshan ophiolite and modern analogs. Gondw. Res. 26, 75–88.
Lepvrier, C., Maluski, H., Van Tich, V., Leyreloup, A., Truong Thi, P., Van Vuong, N., 2004. The early Triassic Indosinian orogeny in Vietnam (Truong Son Belt and Kontum Massif); implications for the geodynamic evolution of Indochina. Tectonophysics 393, 87–118.
Li, X.H., Li, Z.X., Wingate, M.T.D., Chung, S.L., Liu, Y., Lin, G.C., Li, W.X., 2006a. Geochemistry of the 755 Ma Mundine well dyke swarm, northwestern Australia: part of a Neoproterozoic mantle superplume beneath Rodinia? Precambrian Res. 146, 1–15.
Li, X.H., Li, Z.X., Li, W.X., Wang, Y., 2006b. Initiation of the Indosinian Orogeny in South China: evidence for a Permian magmatic arc on Hainan Island. J. Geol. 114, 341–353.
Li, X.-H., Liu, Y., Li, Q.-L., Guo, C.-H., Chamberlain, K.R., 2009. Precise determination of Phanerozoic zircon Pb/Pb age by multicollector SIMS without external standardization. Geochem. Geophys. Geosyst. 10 (n/a-n/a).
Li, Q., Li, X., Liu, Y., Tang, G., Yang, J., Zhu, W., 2010a. Precise U-Pb and Pb-Pb dating of Phanerozoic baddeleyite by SIMS with oxygen flooding technique. J. Anal. At. Spectrom 25, 1107–1113.
Li, X.H., Long, W.G., Li, Q.L., Liu, Y., Zheng, Y.F., Yang, Y.H., Chamberlain, K.R., Wan, D.F., Guo, C.H., Wang, X.C., 2010b. Penglai zircon megacrysts: a potential new working reference material for microbeam determination of Hf–O isotopes and U–Pb age. Geostand. Geoanal. Res. 34, 117–134.
Li, X., Tang, G., Gong, B., Yang, Y.H., Hou, K.J., Hu, Z., Li, Q., Liu, Y., Li, W., 2013. Qinghu zircon:a working reference for microbeam analysis of U-Pb age and Hf and O isotopes. Chin. Sci. Bull. 58, 4647–4654.
Lin, T.-H., Chung, S.-L., Chiu, H.-Y., Wu, F.-Y., Yeh, M.-W., Searle, M.P., Iizuka, Y., 2012. Zircon U–Pb and Hf isotope constraints from the Ailao Shan–Red River shear zone on the tectonic and crustal evolution of southwestern China. Chem. Geol. 291, 23–37.
Liu, C., Deng, J., Liu, J., Shi, Y., 2011. Characteristics of volcanic rocks from late Permian to early Triassic in Ailaoshan tectono-magmatic belt and implications for tectonic settings. Acta Petrol. Sin. 27, 3590–3602.
Liu, J., Tran, M.-D., Tang, Y., Nguyen, Q.-L., Tran, T.-H., Wu, W., Chen, J., Zhang, Z., Zhao, Z., 2012. Permo-Triassic granitoids in the northern part of the Truong Son belt, NW Vietnam: Geochronology, geochemistry and tectonic implications. Gondw. Res. 22, 628–644.
Liu, F., Wang, F., Liu, P., Liu, C., 2013. Multiple metamorphic events revealed by zircons from the Diancang Shan—Ailao Shan metamorphic complex, southeastern Tibetan Plateau. Gondw. Res. 24, 429–450.
Liu, H., Wang, Y., Cawood, P.A., Fan, W., Cai, Y., Xing, X., 2015. Record of Tethyan Ocean closure and Indosinian collision along the Ailaoshan suture zone (SW China). Gondw. Res. 27, 1292–1306.
Liu, H., Wang, Y., Fan, W., Zi, J., Cai, Y., Yang, G., 2014. Petrogenesis and tectonic implications of Late-Triassic high ε Nd(t)-ε Hf(t) granites in the Ailaoshan tectonic zone (SW China). Sci. China Earth Sci. 57 (9), 2181–2194.
Liu, H., Wang, Y., Guo, X., Fan, W., Song, J., 2017a. Late Triassic post-collisional slab breakoff along the Ailaoshan suture: insights from OIB-like amphibolites and associated felsic rocks. Int. J. Earth Sci. 106, 1359–1373.
Liu, H., Wang, Y., Zi, J.-W., 2017b. Petrogenesis of the Dalongkai ultramafic-mafic intrusion and its tectonic implication for the Paleotethyan evolution along the Ailaoshan tectonic zone (SW China). J. Asian Earth Sci. 141, 112–124.
Liu, H., Xia, X., Lai, C.-K., Gan, C., Zhou, Y., Huangfu, P., 2018. Break-away of South China from Gondwana: Insights from the Silurian high-Nb basalts and associated magmatic rocks in the Diancangshan-Ailaoshan fold belt (SW China). Lithos 318-319, 194–208.
McKenzie, D.A.N., O'Nions, R.K., 1991. Partial Melt Distributions from Inversion of rare Earth Element Concentrations. J. Petrol. 32, 1021–1091.
Metcalfe, I., 2013. Gondwana dispersion and Asian accretion: Tectonic and palaeogeographic evolution of eastern Tethys. J. Asian Earth Sci. 66, 1–33.
Moyen, J.F., Laurent, O., Chelle-Michou, C., Couzinié, S., Vanderhaeghe, O., Zeh, A., Villaros, A., Gardien, V., 2017. Collision vs. subduction-related magmatism: two contrasting ways of granite formation and implications for crustal growth. Lithos 277, 154–177.
Pilet, S., Baker, M.B., Müntener, O., Stolper, E.M., 2011. Monte Carlo simulations of metasomatic enrichment in the lithosphere and implications for the source of alkaline basalts. J. Petrol. 52, 1415–1442.
Plank, T., Langmuir, C.H., 1998. The chemical composition of subducting sediment and its consequences for the crust and mantle. Chem. Geol. 145, 325–394.
Plank, T., Kelley, K.A., Murray, R.W., Stern, L.Q., 2007. Chemical composition of sediments subducting at the Izu-Bonin trench. Geochem. Geophys. Geosyst. 8.
Qi, X., Zeng, L., Zhu, L., Hu, Z., Hou, K., 2012. Zircon U–Pb and Lu–Hf isotopic systematics of the Daping plutonic rocks: implications for the Neoproterozoic tectonic evolution of the northeastern margin of the Indochina block, Southwest China. Gondw. Res. 21, 180–193.
Qin, X.F., Wang, Z.Q., Zhang, Y.L., Pan, L.Z., Hu, G.A., Zhou, F.S., 2011. Geochronology and geochemistry of early Mesozoic acid volcanic rocks from Southwest Guangxi: constraints on tectonic evolution of the southwestern segment of Qinzhou-Hangzhou joint belt. Acta Petrol. Sin. 27, 794–808.
Qin, X.F., Wang, Z., Zhang, Y., Pan, L., Hu, G., Zhou, F., 2012. Geochemistry of Permian Mafic Igneous Rocks from the Napo-Qinzhou Tectonic Belt in Southwest Guangxi, Southwest China: Implications for Arc-Back Arc Basin Magmatic Evolution. Acta Geol. Sin. (Engl. Ed.) 86, 1182–1199.
Rapp, R.P., Watson, E.B., 1995. Dehydration Melting of Metabasalt at 8–32 kbar: Implications for Continental Growth and Crust-Mantle Recycling. J. Petrol. 36, 891–931.
Rudnick, R., Gao, S., 2003. Composition of the continental crust. Treat. Geochem. 3, 1–64.
Segal, I., Halicz, L., Platzner, I.T., 2003. Accurate isotope ratio measurements of ytterbium by multiple collection inductively coupled plasma mass spectrometry applying erbium and hafnium in an improved double external normalization procedure. J. Anal. At. Spectrom 18, 1217–1223.
Shellnutt, J.G., Zhou, M.-F., Zellmer, G.F., 2009. The role of Fe-Ti oxide crystallization in the formation of A-type granitoids with implications for the Daly gap: an example from the Permian Baima igneous complex, SW China. Chem. Geol. 259 (3–4), 204–217.
Singer, B.S., Myers, J.D., Frost, C.D., 1992. Mid-Pleistocene lavas from the Seguam volcanic center, central Aleutian arc: closed-system fractional crystallization of a basalt to rhyodacite eruptive suite. Contrib. Mineral. Petrol. 110 (1), 87–112.
Sivell, W., Waterhouse, J., 1988. Petrogenesis of Gympie Group volcanics: evidence for remnants of an early Permian volcanic arc in eastern Australia. Lithos 21, 81–95.
Sláma, J., Košler, J., Condon, D.J., Crowley, J.L., Gerdes, A., Hanchar, J.M., Horstwood, M.S.A., Morris, G.A., Nasdala, L., Norberg, N., Schaltegger, U., Schoene, B., Tubrett, M.N., Whitehouse, M.J., 2008. Plešovice zircon-a new natural reference material for U–Pb and Hf isotopic microanalysis. Chem. Geol. 249, 1–35.
Su, Y.J., 2002. Mid-Ocean Ridge Basalt Trace Element Systematics: Constraints from Database Management, ICP-MS Analyses, Global Data Compilation, and Petrologic Modeling. Columbia University.

Sun, S.-S., McDonough, W., 1989. Chemical and isotopic systematics of oceanic basalts: implications for mantle composition and processes. Geol. Soc. Lond. Spec. Publ. 42, 313–345.
Tollstrup, D.L., Gill, J.B., 2005. Hafnium systematics of the Mariana arc: evidence for sediment melt and residual phases. Geology 33, 737–740.
Valley, J.W., Kita, N.T., 2009. In situ oxygen isotope geochemistry by ion microprobe. MAC Short Course 41, 19–63.
Valley, J., Lackey, J., Cavosie, A., Clechenko, C., Spicuzza, M., Basei, M., Bindeman, I., Ferreira, V., Sial, A., King, E., 2005. 4.4 billion years of crustal maturation: oxygen isotope ratios of magmatic zircon. Contrib. Mineral. Petrol. 150, 561–580.
Wang, X., Metcalfe, I., Jian, P., He, L., Wang, C., 2000. The Jinshajiang–Ailaoshan Suture Zone, China:tectonostratigraphy,age and evolution. J. Asian Earth Sci. 18, 675–690.
Wang, Y., Qian, X., Cawood, P.A., Liu, H., Feng, Q., Zhao, G., Zhang, Y., He, H., Zhang, P., 2018. Closure of the East Paleotethyan Ocean and amalgamation of the Eastern Cimmerian and Southeast Asia continental fragments. Earth Sci. Rev. 186, 195–230.
Wang, Z.L., Xu, D., Wu, C., Fu, W., Wang, L., Wu, J., 2013. Discovery of the late Paleozoic Ocean island basalts(OIB) in Hainan Island and their geodynamic implications. Acta Petrol. Sin. 29, 875–886.
Wang, Q., Deng, J., Li, C., Li, G., Yu, L., Qiao, L., 2014. The boundary between the Simao and Yangtze blocks and their locations in Gondwana and Rodinia: Constraints from detrital and inherited zircons. Gondw. Res. 26, 438–448.
Wang, D., Guo, J.-H., Qian, Q., Fu, B., 2018. Formation of late Archean high-$\delta^{18}O$ diorites through partial melting of hydrated metabasalts. J. Petrol. 59, 419–446.
Wei, Q., Shen, S., 1997. Arc volcanic rocks of late Permian (P2) in Taizhong-Lixianjiang zone, Ailao Shan area. J. Mineral. Petrol. 17, 8–16.
Workman, R.K., Hart, S.R., 2005. Major and trace element composition of the depleted MORB mantle (DMM). Earth Planet. Sci. Lett. 231, 53–72.
Wu, W., Liu, J., Chen, X., Zhang, L., 2016. Zircon U–Pb ages, Hf isotope data, and tectonic implications of Early–Middle Triassic granitoids in the Ailaoshan high-grade metamorphic belt of Southeast Tibet. Int. J. Earth Sci. 1–23.
Xia, X., Nie, X., Lai, C.K., Wang, Y., Long, X., Meffre, S., 2016. Where was the Ailaoshan Ocean and when did it open: a perspective based on detrital zircon U–Pb age and Hf isotope evidence. Gondw. Res. 36, 488–502.
Xia, X.-P., Xu, J., Huang, C., Long, X., Zhou, M., 2019. Subduction Polarity of the Ailaoshan Ocean (Eastern Paleotethys): Constraints from Detrital Zircon U-Pb and Hf-O Isotopes for the Longtan Formation (GSA Bulletin).
Xu, J.-F., Castillo, P.R., 2004. Geochemical and Nd–Pb isotopic characteristics of the Tethyan asthenosphere: implications for the origin of the Indian Ocean mantle domain. Tectonophysics 393, 9–27.
Xu, J., Xia, X., Lai, C., Long, X., Huang, C., 2019a. When did the Paleotethys Ailaoshan Ocean close: new insights from detrital zircon U-Pb age and Hf isotopes. Tectonics 38, 1798–1823.
Xu, J., Xia, X., Huang, C., Cai, K., Yin, C., Lai, C.-K., 2019b. Changes of provenance of Permian and Triassic sedimentary rocks from the Ailaoshan suture zone (SW China) with implications for the closure of the eastern Paleotethys. J. Asian Earth Sci. 170, 234–248.
Xu, J., Xia, X.-P., Lai, C.-K., Zhou, M., Ma, P., 2019c. First Identification of late Permian Nb-Enriched Basalts in Ailaoshan Region (SW Yunnan, China): Contribution from Emeishan Plume to Subduction of Eastern Paleotethys. Geophys. Res. Lett. 46, 2511–2523.
Yin, A., Harrison, T.M., 2000. Geologic evolution of the Himalayan-Tibetan orogen. Annu. Rev. Earth Planet. Sci. 28, 211–280.
YNGMR, 1990. Regional Geology of Yunnan Province. Geological Publishing House, Beijing.
Zhang, L., Ren, Z.Y., Nichols, A.R.L., Zhang, Y.H., Zhang, Y., Qian, S.P., Liu, J.Q., 2014a. Lead isotope analysis of melt inclusions by LA-MC-ICP-MS. J. Anal. At. Spectrom 29, 1393–1405.
Zhang, R.Y., Lo, C.H., Li, X.H., Chung, S.L., Anh, T.T., Tri, T.V., 2014b. U-Pb dating and tectonic implication of ophiolite and metabasite from the Song Ma suture zone, northern Vietnam. Am. J. Sci. 314, 649–678.
Zhang, L., Ren, Z.Y., Xia, X.P., Li, J., Zhang, Z.F., 2015. IsotopeMaker: A Matlab program for isotopic data reduction. International Journal of Mass Spectrometry 392, 118–124.
Zhang, B., Yin, C., Zhang, J., Wang, J., Zhong, D., Wang, Y., Lai, Q., Yue, Y., Zhou, Q., 2017. Midcrustal shearing and doming in a Cenozoic compressive setting along the Ailao Shan-Red River shear zone. Geochem. Geophys. Geosyst. 18, 400–433.
Zhu, J.-J., Hu, R.-Z., Bi, X.-W., Zhong, H., Chen, H., 2011. Zircon U–Pb ages, Hf–O isotopes and whole-rock Sr–Nd–Pb isotopic geochemistry of granitoids in the Jinshajiang suture zone, SW China: Constraints on petrogenesis and tectonic evolution of the Paleo-Tethys Ocean. Lithos 126, 248–264.
Zi, J.-W., Cawood, P.A., Fan, W.-M., Wang, Y.-J., Tohver, E., McCuaig, T.C., Peng, T.-P., 2012. Triassic collision in the Paleo-Tethys Ocean constrained by volcanic activity in SW China. Lithos 144-145, 145–160.